Modulation of gauge field for the parity-time phase transition in circuit QED

Genting Dai,[1,*] Yongcheng He,[1] Kaiyong He,[1] Liangliang Yang,[1] Jianshe Liu,[1] and Wei Chen[1,2,3,†]

[1]*Laboratory of Superconducting Quantum Information Processing, School of Integrated Circuits, Tsinghua University, Beijing 100084, China*

[2]*Beijing Innovation Center for Future Chips, Tsinghua University, Beijing 100084, China*

[3]*Beijing National Research Center for Information Science and Technology, Beijing 100084, China*

(Received 17 October 2023; revised 22 January 2024; accepted 7 March 2024; published 25 March 2024)

In this work, a parity-time ($\mathcal{PT}$)-symmetric system is investigated based on superconducting circuits, which allows the tunability of atom-atom coupling using superconducting qubits. The calculation results demonstrate that the interaction between artificial atoms significantly impacts the transmission spectrum and the conditions of the phase transition in the system. When introducing a weak probe signal into the $\mathcal{PT}$-symmetric system, several findings are observed. (1) The symmetry and intensity of both the linear and nonlinear outputs can be fine-tuned by adjusting the coupling strength between artificial atoms or manipulating the gauge-invariant phase in the system. (2) Nonreciprocal transmission can be achieved by driving different cavity modes. (3) The exceptional point (EP) of the $\mathcal{PT}$ phase transition can be adjusted within a certain range by modifying the gauge-invariant phase or adjusting the coupling strength in the system. One feasible experimental setup is also described and analyzed based on existing experimental techniques. These findings may inspire further research into modulating quantum phase transitions based on superconducting circuits.

DOI: 10.1103/PhysRevA.109.033723

I. INTRODUCTION

The study of phase transition modulation has garnered significant attention in modern physics in recent years [1–18]. Notable efforts addressing phase transition modulation have been conducted across diverse physical platforms. For example, carrier concentration in ultrathin materials [5] and double-pulse excitation [6] have been studied for metal-insulator transitions in superconductivity mechanisms. Gate voltage adjustments control the 0 - π phase transition in topological insulators [7]. The manipulation of topological phase transitions within magnonic topological phases involves research into magnon-magnon interaction [8], magnon-phonon coupling [9–11], and variation of magnetic field [12–14]. For the ferroelectric transition in distinct magnetoelectric materials, exploration includes the use of magnetic fields [15,16], electric field [17], and temperature variations [18].

The notion of parity-time ($\mathcal{PT}$) symmetry has been studied in many branches of physics, including optics [19–24], acoustics [25–27], electronic circuits [28–32], and photonics [33–38], among others. Due to the mathematical relationship between quantum mechanics and optics, photonics systems serve as excellent platforms for $\mathcal{PT}$ symmetry research. A fundamental architecture comprises two coupled cavities exhibiting non-Hermiticity due to gain and loss [39–41]. In such systems, the phase transition can lead to supermode profiles, where the real frequency components become complex. By crossing the exceptional point (EP) in parameter space, the eigenvalue spectra transition from real to complex, causing the corresponding modes to merge into one [33,42–45]. The $\mathcal{PT}$ phase transition exhibits intriguing and counterintuitive properties, especially in proximity to the EP, leading to significant transformations in system dynamics. The distinctive attributes of $\mathcal{PT}$-symmetric phase transitions hold promise for applications across various fields, including loss-induced or gain-induced transparency [46–49], low-power optical isolation [50–52], unidirectional invisibility [53–58], and more. The EP, situated in parameter space with unique properties, marks significant changes in system behavior upon crossing it. Meeting the conditions for EP occurrence poses notable challenges, thereby complicating the experimental realization of $\mathcal{PT}$-symmetric systems. Controlled manipulation of EPs could alleviate these challenges, enabling enhanced control and utilization of $\mathcal{PT}$-symmetric system characteristics. However, only a limited number of studies have proposed methods to modulate $\mathcal{PT}$ phase transitions for increased flexibility in the process [59–62].

In this work, we introduce a method that leverages the nontrivial gauge phase to modulate the $\mathcal{PT}$ phase transition within the system. To illustrate this approach, a cavity-QED system can be established using either a $\mathcal{PT}$-symmetric microcavity with classical atoms or one based on superconducting circuits [63,64]. The phase associated with cavity-cavity coupling is examined as a nontrivial gauge phase of the overall system [65–67]. This phase can be manipulated by adjusting the magnetic flux passing through the coupler [68–70]. To examine the influence of the nontrivial gauge phase and atom-atom coupling on the phase transition, an analysis of the linear and nonlinear characteristics based on the output field of a weak probe signal is conducted for various

*dgt20@mails.tsinghua.edu.cn

†weichen@mail.tsinghua.edu.cn

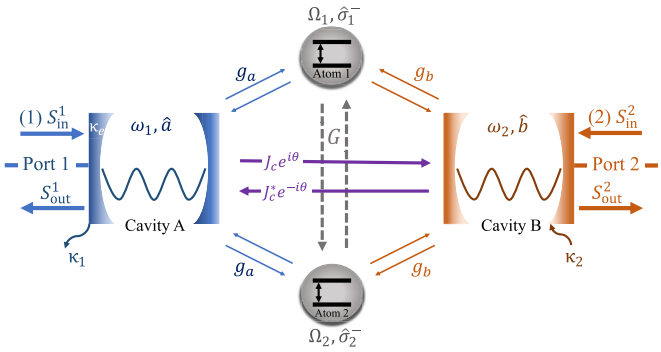

FIG. 1. Schematic diagram of a $\mathcal{PT}$-symmetric system, including two cavity modes $\hat{a}$ and $\hat{b}$ with gain and loss, two atoms $\hat{\sigma}_1^{\pm}$ and $\hat{\sigma}_2^{\pm}$ regarded as two two-level systems. Within the system, the cavity-cavity coupling strength is denoted as $Je^{i\theta}$, the atom-cavity coupling strengths are g_a and g_b, and the atom-atom coupling strength is represented by G. Cavity A can be externally driven by a probe field $S_{\rm in}^1$ with amplitude ϵ_p and frequency ω_p at port 1, with the resulting field $S_{\rm out}^1$ serving as the output of the driving field. Meanwhile, cavity B can be driven by an external probe field $S_{\rm in}^2$ at port 2, and the corresponding output field is denoted as $S_{\rm out}^2$.

scenarios [71–73]. Utilizing the steady-state approximation enables the calculation of the eigenvalue spectrum. Our results indicate the significant impact of both the nontrivial gauge phase and atom-atom coupling on the symmetry and intensity of the output field. Moreover, the phase and coupling strength of the interactions between cavities or atoms are shown to play a pivotal role in modulating the EP of the phase transition within the system.

This paper is organized as follows. In Sec. III B, we delve deeper into the cavity-atom system with $\mathcal{PT}$ symmetry, a model that offers significant insights into the underlying physics of $\mathcal{PT}$-symmetric systems. In Sec. III C, two kinds of systems are introduced in the first part, focusing on the analytical description of the linear transmission rate and the third-order Kerr-nonlinear coefficient of the output field. An analysis of realizing nonreciprocal transmission in the system is conducted through numerical calculations. In the second part, the phase diagram of the $\mathcal{PT}$-symmetric system is calculated based on the steady-state approximation. In the third part, we demonstrate that the EP of the phase transition can be modulated by the nontrivial gauge phase and coupling strength in the system. In Sec. V, an experimental setup utilizing a superconducting circuit is proposed to investigate the system under consideration. Additionally, a table containing parameters from some existing experiments is compiled. Finally, some remarks on this work are summarized in Sec. IV.

II. THEORETICAL MODEL AND ANALYTIC METHODS

As depicted in Fig. 1, a $\mathcal{PT}$-symmetric system is constructed, comprising two coupled single-mode cavities and two atoms. Cavities A and B are represented by bosonic annihilation and creation operators $(\hat{a}, \hat{a}^\dagger)$ with resonant frequency ω_1 and decay rate κ_1, and $(\hat{b}, \hat{b}^\dagger)$ with resonant frequency ω_2 and decay rate κ_2, respectively. Atoms 1 and 2 are modeled as two-level systems, represented by Pauli operators $\hat{\sigma}_1^{\pm}$ with frequency Ω_1 and decay rate γ_1, and $\hat{\sigma}_2^{\pm}$ with frequency Ω_2 and decay rate γ_2, respectively. Cavity A is passive (i.e., loss), and cavity B is active (i.e., gain). The two cavities are coupled via a tunable coupling strength J with phase θ [68–70]. The two atoms are coupled to the two cavities with coupling strength g. The first physical system is established with microcavities and classical atoms. The second physical system is realized using superconducting circuits, employing superconducting qubits as artificial atoms [64].

To investigate the signal transmission process, each of the two cavities can be individually stimulated. Specifically, at port 1, cavity A is excited by a weak external probe field denoted as $S_{\rm in}^1$, characterized by an amplitude ϵ_p and frequency ω_p. The parameter κ_e represents the coupling loss rate between the cavity and the external field, which is intricately tied to the coupling quality factor [45]. The total decay rate of cavity A is a sum of the intrinsic loss rate and the external loss rate, given by $\kappa_a = \kappa_1 + \kappa_e$, while cavity B possesses a decay rate of $\kappa_b = \kappa_2$. Conversely, at port 2, the probe signal is introduced into cavity B. Consequently, the overall decay rate of cavity B is denoted as $\kappa_b' = \kappa_2 + \kappa_e$, while cavity A sustains a decay rate of $\kappa_a' = \kappa_1$. For simplicity, we assume that $\omega_1 = \omega_2 = \omega$, $\Omega_1 = \Omega_2 = \Omega$, $\gamma_1 = \gamma_2$, and $S_{\rm in}^1 = S_{\rm in}^2 = S_{\rm in}$. The coupling strengths J, g, and G are considered as real numbers. Following the formalism of Blais *et al.* [64], the Hamiltonian for this composite system, involving a driving probe field targeted as cavity A, is expressed as (setting $\hbar = 1$)

$$\begin{aligned}\hat{H} &= \hat{H}_0 + \hat{H}_1 + \hat{H}_d \\ &= \omega(\hat{a}^\dagger\hat{a} + \hat{b}^\dagger\hat{b}) + \Omega(\hat{\sigma}_1^+\hat{\sigma}_1^- + \hat{\sigma}_2^+\hat{\sigma}_2^-) \\ &\quad + g(\hat{a}\hat{\sigma}_1^+ + \hat{a}^\dagger\hat{\sigma}_1^-) + g(\hat{a}\hat{\sigma}_2^+ + \hat{a}^\dagger\hat{\sigma}_2^-) \\ &\quad + g(\hat{b}\hat{\sigma}_1^+ + \hat{b}^\dagger\hat{\sigma}_1^-) + g(\hat{b}\hat{\sigma}_2^+ + \hat{b}^\dagger\hat{\sigma}_2^-) \\ &\quad + G(\hat{\sigma}_1^+\hat{\sigma}_2^- + \hat{\sigma}_1^-\hat{\sigma}_2^+) \\ &\quad + J(e^{i\theta}\hat{a}^\dagger\hat{b} + e^{-i\theta}\hat{a}\hat{b}^\dagger) + i\sqrt{\kappa_e}[S_{\rm in}(t)\hat{a}^\dagger - S_{\rm in}^*(t)\hat{a}]. \quad (1)\end{aligned}$$

The first two terms in the expression signify the energy associated with the uncoupled cavity-atom system. Subsequently, the third to sixth terms encapsulate the interactions arising from the cavity-atom coupling, while the seventh and eighth terms delineate the dynamics stemming from the cavity-cavity coupling and atom-atom couplings. The final term illustrates the scenario where cavity A is stimulated by a probe field. In this context, a passive cavity exhibits an intrinsic decay rate denoted as $\kappa_j > 0$, whereas an active cavity is characterized by $\kappa_j < 0$. These rates adhere to the condition $|\kappa_j| = \omega_j/Q_j$ $(j = 1, 2)$, where Q_1 and Q_2 represent the intrinsic quality factors of cavities A and B, respectively. As for the external loss rate κ_e, it is governed by the relationship $|\kappa_e| = \omega_j/Q_e$ $(j = 1, 2)$, where Q_e signifies the coupling quality factor of either cavity A or B [45]. The overall decay rate of the cavity is a composite of the intrinsic loss rate and the external loss rate.

To facilitate the transformation of the Hamiltonian presented in Eq. (1) into the rotating frame with respect to the external probe signal operating at the frequency ω_p, $\hat{H}_{\rm free}$ and

$U(t)$ are defined:

$$\hat{H}_{\text{free}} = \omega_p(\hat{a}^\dagger\hat{a} + \hat{b}^\dagger\hat{b} + \hat{\sigma}_1^+\hat{\sigma}_1^- + \hat{\sigma}_2^+\hat{\sigma}_2^-), \tag{2}$$

$$U(t) = e^{-i\hat{H}_{\text{free}}t}. \tag{3}$$

The Hamiltonian $\hat{H}_{\text{rot}}$ under rotating frame is

$$\hat{H}_{\text{rot}} = \Delta(\hat{a}^\dagger\hat{a} + \hat{b}^\dagger\hat{b}) + (\Delta+\delta)(\hat{\sigma}_1^+\hat{\sigma}_1^- + \hat{\sigma}_2^+\hat{\sigma}_2^-) + \hat{H}_{\text{I}} + \hat{H}_{\text{d}}, \tag{4}$$

where $\Delta = \omega - \omega_p$ signifies the frequency detuning existing between the cavity and the probe signal, while $\delta = \Omega - \omega$ represents the frequency detuning between the atoms and cavity modes. The term $\hat{H}_{\text{I}}$ embodies the interactions encompassing cavity-atom, cavity-cavity, and atom-atom couplings. The term $\hat{H}_{\text{d}} = i\sqrt{\kappa_e}(\epsilon_p\hat{a}^\dagger - \epsilon_p^*\hat{a})$ characterizes the driving of cavity 1 by the probe signal, with ϵ_p denoting the classical amplitude of the probe field. Notably, the amplitude ϵ_p is correlated with the signal power P_{in} according to $|\epsilon_p| = \sqrt{P_{\text{in}}/\omega_p}$.

Under such a low-power driving field, the input-output relationship in the system can be described by the semiclassical Heisenberg-Langevin equations of motion derived from the Heisenberg-Langevin formalism [74,75]:

$$\frac{da}{dt} = -\left(i\Delta + \frac{\kappa_a}{2}\right)a - Je^{i(\frac{\pi}{2}+\theta)}b - ig(\hat{\sigma}_1^- + \hat{\sigma}_2^-) + \epsilon_p\sqrt{\kappa_e}, \tag{5}$$

$$\frac{db}{dt} = -\left(i\Delta + \frac{\kappa_b}{2}\right)b - Je^{i(\frac{\pi}{2}-\theta)}a - ig(\hat{\sigma}_1^- + \hat{\sigma}_2^-), \tag{6}$$

$$\frac{d\sigma_1^z}{dt} = -\gamma\left(\sigma_1^z + \frac{1}{2}\right) - ig(a\sigma_1^+ - a^\dagger\sigma_1^-) - ig(b\sigma_1^+ - b^\dagger\sigma_1^-) - iG(\sigma_2^-\sigma_1^+ - \sigma_2^+\sigma_1^-), \tag{7}$$

$$\frac{d\sigma_1^-}{dt} = -\left[i(\Delta+\delta) + \frac{\gamma}{2}\right]\sigma_1^- + 2i[g(a+b) + G\sigma_2^-]\sigma_1^z, \tag{8}$$

$$\frac{d\sigma_2^z}{dt} = -\gamma\left(\sigma_2^z + \frac{1}{2}\right) - ig(a\sigma_2^+ - a^\dagger\sigma_2^-) - ig(b\sigma_2^+ - b^\dagger\sigma_2^-) - iG(\sigma_1^-\sigma_2^+ - \sigma_1^+\sigma_2^-), \tag{9}$$

$$\frac{d\sigma_2^-}{dt} = -\left[i(\Delta+\delta) + \frac{\gamma}{2}\right]\sigma_2^- + 2i[g(a+b) + G\sigma_1^-]\sigma_2^z. \tag{10}$$

Consider system operators $\hat{o}_1$ and $\hat{o}_2$, where $\langle\hat{o}_1\rangle = o_1$ and $\langle\hat{o}_2\rangle = o_2$. Consequently, o_1 and o_2 are observable, and the mean-field approximation is given by $\langle\hat{o}_1\hat{o}_2\rangle = \langle\hat{o}_1\rangle\langle\hat{o}_2\rangle$ [45]. In the context of two-level atoms, designate the ground state as $|0\rangle$ and the excited state as $|1\rangle$. It follows that $\hat{\sigma}_j^+ = |1\rangle\langle 0|$, $\hat{\sigma}_j^- = |0\rangle\langle 1|$, and $\hat{\sigma}_j^z = (\langle\hat{\sigma}_j^+\hat{\sigma}_j^-\rangle - \langle\hat{\sigma}_j^-\hat{\sigma}_j^+\rangle)/2$ $(j = 1, 2)$ signifies the half-population difference between the ground and excited states.

In the realm of quantum mechanics perturbation theory, this methodology can be extended to two cavity modes. Under the assumption of weak excitation, it can also be employed for two atoms (the justification for these approximation methods is deliberated in the initial section in Appendix A). The terms of the perturbation expansions are [76–79]

$$a = \lambda a^{(1)} + \lambda^2 a^{(2)} + \lambda^3 a^{(3)} + \cdots, \tag{11}$$

$$b = \lambda b^{(1)} + \lambda^2 b^{(2)} + \lambda^3 b^{(3)} + \cdots, \tag{12}$$

$$\sigma_i^z = \sigma_i^{z(0)} + \lambda\sigma_i^{z(1)} + \lambda^2\sigma_i^{z(2)} + \lambda^3\sigma_i^{z(3)} + \cdots, \tag{13}$$

$$\sigma_i^- = \sigma_i^{-(0)} + \lambda\sigma_i^{-(1)} + \lambda^2\sigma_i^{-(2)} + \lambda^3\sigma_i^{-(3)} + \cdots, \tag{14}$$

in which $\lambda \in [0, 1]$, and $i = 1, 2$. It is assumed that $a^{(0)} = b^{(0)} = 0$ since the weak probe field drives the two cavities. Furthermore, due to the presence of zeroth-order electronic operators, $\sigma_1^{-(0)} = \sigma_2^{-(0)} = 0$. With respect to the definition of $\hat{\sigma}_j^z$, $(j = 1, 2)$ $\sigma_1^{z(0)} = \sigma_2^{z(0)} = -1/2$. Then it becomes feasible to compute each cavity field term under these particular approximations.

III. MAIN RESULTS

A. Linear and nonlinear output properties

By employing Eqs. (11)–(14) to address the semiclassical Heisenberg-Langevin equations presented in Eqs. (5)–(10), one can determine the field amplitudes in cavity A and cavity B for various systems. When cavity A is stimulated, the output signal S_{out} is defined as

$$S_{\text{out}} = S_{\text{in}} - \sqrt{\kappa_e}a. \tag{15}$$

Upon truncating the cavity field terms to third order, the resulting output field is given by

$$S_{\text{out}} = \epsilon_p - \sqrt{\kappa_e}a^{(1)} - \sqrt{\kappa_e}a^{(2)} - \sqrt{\kappa_e}a^{(3)}. \tag{16}$$

Then, each term of the cavity field can be computed based on the system parameters.

1. Coupled double microcavities with atoms

In the first physical system, the setup comprises two microcavities and two classical atoms. There is no coupling between the atoms, implying $G = 0$. By solving the aforementioned equations, the first three terms of the field in cavity A can be derived as follows:

$$a_I^{(1)} = \frac{\epsilon_p\sqrt{\kappa_e}d_2}{d_1d_2 - d_3d_4}, \tag{17}$$

$$a_I^{(2)} = 0, \tag{18}$$

$$a_I^{(3)} = \frac{4g^4(d_2-d_3)(d_2-d_4)}{(d_1d_2-d_3d_4)^2}\left|\frac{\sqrt{\kappa_e}(d_2-d_4)}{d_1d_2-d_3d_4}\right|^2 \times \frac{\sqrt{\kappa_e}\epsilon_p|\epsilon_p|^2}{[\gamma/2 + i(\Delta+\delta)][\gamma^2/4 + (\Delta+\delta)^2]}, \tag{19}$$

in which $d_1 = (i\Delta + \kappa_1/2 + \kappa_e/2) + M_1$, $d_2 = (i\Delta + \kappa_2/2) + M_1$, $d_3 = Je^{i(\pi/2+\theta)} + M_1$, $d_4 = Je^{i(\pi/2-\theta)} + M_1$, and $M_1 = 2g^2/[\gamma/2 + i(\Delta+\delta)]$. The nonzero terms of the field intensity in cavity A are directly linked to the intensity of input driving field ϵ_p. When analyzing the transmission behavior of the $\mathcal{PT}$-symmetric system, the coefficients governing the linear transmission rate $\chi^{(1)}$ and the third-order

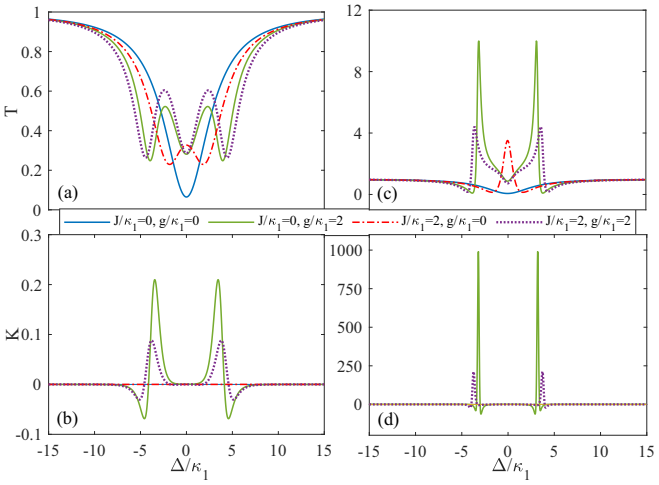

FIG. 2. The linear transmission rate T and Kerr-nonlinear coefficient K of the probe field vs the detuning Δ/κ_1 for various parameter sets $(J/\kappa_1,\ g/\kappa_1,\ \kappa_2/\kappa_1)$. The gain-to-loss ratios are specified as (a and b) $\kappa_2/\kappa_1 = 3.6$ and (c and d) $\kappa_2/\kappa_1 = -3.6$. The curves are denoted by different colors and line styles: blue solid, green solid, red dash-dot, and purple dotted lines correspond to $J/\kappa_1 = 0$, $g/\kappa_1 = 0$; $J/\kappa_1 = 0$, $g/\kappa_1 = 2$; $J/\kappa_1 = 2$, $g/\kappa_1 = 0$; and $J/\kappa_1 = 2$, $g/\kappa_1 = 2$, respectively. The remaining parameters are fixed as $\kappa_e = 5\kappa_1$, $\gamma = 0.2\kappa_1$, $\delta = 0$, and $\theta = \pi/2$.

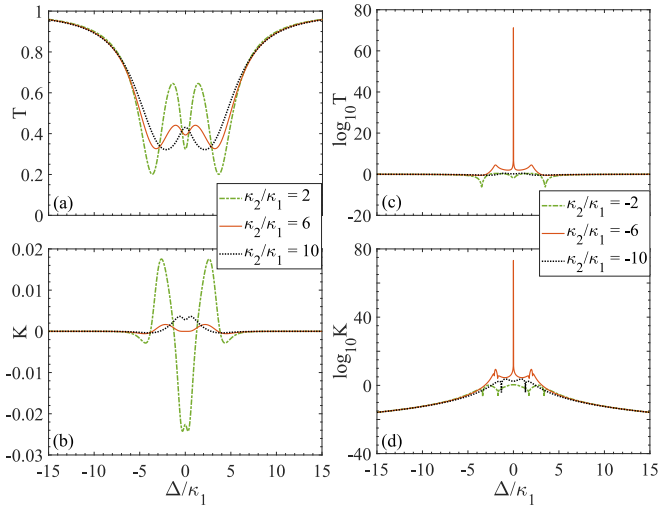

FIG. 3. The linear transmission rate T and Kerr-nonlinear coefficient K of the probe field vs detuning Δ/κ_1 for different values of κ_2/κ_1. Considering the passive-passive double-cavity system, (a) the linear transmission rate T for $\kappa_2 = 2\kappa_1$ (green dash-dot line), $\kappa_2 = 6\kappa_1$ (red solid line), $\kappa_2 = 10\kappa_1$ (black dotted line). (b) Kerr-nonlinear coefficient K for the same κ_2/κ_1 values. Shifting focus to the passive-active double-cavity system, (c) the logarithm of T for $\kappa_2 = -2\kappa_1$ (green dash-dot line), $\kappa_2 = -6\kappa_1$ (red solid line), $\kappa_2 = -10\kappa_1$ (black dotted line). (d) The logarithm of K for the same values of κ_2/κ_1. The remaining parameters in the system are defined as $J = 3\kappa_1$, $g = \kappa_1$, $\kappa_e = 5\kappa_1$, $\gamma = 0.7\kappa_1$, $\delta = 0$, and $\theta = \pi/2$.

Kerr coefficient $\chi^{(3)}$ can be defined in accordance with nonlinear optics [79]:

$$\chi^{(1)} = 1 - a^{(1)}/\epsilon_p, \tag{20}$$

$$\chi^{(3)} = a^{(3)}/(\epsilon_p|\epsilon_p|^2). \tag{21}$$

Within the system, $T = |\chi^{(1)}|^2$ quantifies the intensity of the normalized linear transmission rate. Concerning the coefficient $\chi^{(3)}$, the real part $K = \mathrm{Re}[\chi^{(3)}]$ characterizes the Kerr nonlinearity, while the imaginary part $A = \mathrm{Im}[\chi^{(3)}]$ is associated with nonlinear absorption. Based on the transmission coefficients delineated in Eqs. (20) and (21), the impact from the intensity of the probe field may be neglected.

In units of κ_1, the normalized linear transmission $T = |\chi^{(1)}|^2$ of the probe signal is depicted as a function of detuning Δ/κ_1 in Fig. 2, considering four types of coupling interactions: (1) no coupling $(J = 0, g = 0)$, (2) direct coupling $(J \neq 0, g = 0)$, (3) indirect coupling $(J = 0, g \neq 0)$, and (4) both direct and indirect coupling $(J \neq 0, g \neq 0)$. In Figs. 2(a) and 2(b), the decay rates of the two cavities satisfy $\kappa_2/\kappa_1 = 3.6$. When $J/\kappa_1 = 0$, $g/\kappa_1 = 0$ (blue solid line) in Fig. 2, the system reduces to a single cavity, and the linear transmission rate T displays a dip at $\Delta = 0$, matching the probe field frequency with the cavity resonant frequency. Conversely, for $J/\kappa_1 = 2$, $g/\kappa_1 = 0$ (red dashed line), the system transforms into a passive-passive double-cavity system, featuring dipole-induced transparency (DIT) in the linear transmission [80–84]. The green solid line and purple dotted line correspond to scenarios where the system comprises two cavities and two atoms. One system exhibits indirect coupling between cavities, while the other involves both indirect and direct coupling. These configurations still exhibit DIT features but with three absorption dips, owing to the interactions between cavities and atoms introducing additional resonant modes, resulting in extra absorption dips within the linear transmission rate curve. In Fig. 2(b), the absence of a nonlinear output signal when $g = 0$ indicates that the nonlinearity in the system arises from the qubits. In Figs. 2(c) and 2(d), with $\kappa_2/\kappa_1 = -3.6$, the linear transmission rates for $J/\kappa_1 = 0$, $g/\kappa_1 = 0$ (blue solid line) remain consistent with Fig. 2(a), representing a single cavity system. Conversely, for $J/\kappa_1 = 2$, $g/\kappa_1 = 0$ (red dashed line), a passive-active double-cavity system is established, exhibiting an enhanced inverted-DIT profile, featuring a pronounced transmission peak at $\Delta = 0$ [49]. In the remaining cases (green solid line and purple dotted line), a similar enhanced inverted-DIT profile is also observed, where two symmetrical peaks emerge around $\Delta = 0$. In Fig. 2(d), the K significantly amplifies due to the gain in cavity B.

In Fig. 3, the linear transmission rate $T = |\chi^{(1)}|^2$ and the third-order Kerr-nonlinear coefficient $K = \mathrm{Re}[\chi^{(3)}]$ are plotted for both passive-passive and passive-active double-cavity systems. For the setup comprising two passive cavities and two atoms, the cavity gain-to-loss ratio is characterized by $\kappa_2/\kappa_1 > 0$. The linear output T is plotted against the detuning Δ/κ_1 in Fig. 3(a). When $\kappa_2/\kappa_1 = 2$, three absorption dips are evident in the linear transmission rate curve. With an increase in the gain-to-loss ratio κ_2/κ_1, a transparent window emerges at $\Delta = 0$, accompanied by double-symmetric-sideband absorption dips. The third-order Kerr coefficient K is graphed against the detuning Δ/κ_1 in Fig. 3(b). These curves exhibit symmetry around $\Delta = 0$, and the system manifests weak nonlinear output when $\kappa_2/\kappa_1 > 0$. In scenarios where cavity A is passive and cavity B holds gain, denoted by $\kappa_2/\kappa_1 < 0$.

The logarithm of the linear output T as a function of Δ/κ_1 is shown in Fig. 3(c), showcasing an inverted-DIT transparency profile in the linear output. With the gain-to-loss ratio transitioning from $\kappa_2/\kappa_1 = -2$ to $\kappa_2/\kappa_1 = -6$, there is a progressive rise in the amplitude of the linear output. Three amplifying peaks become discernible, notably with the peak at $\Delta = 0$ exhibiting greater prominence than others. As κ_2/κ_1 reaches -10, the amplitudes of the sideband peaks are diminished, and the peak at $\Delta = 0$ vanishes. In Fig. 3(d), the logarithm of the nonlinear output K is graphed against Δ/κ_1. Mirroring the behavior of the linear output, there is a noteworthy enhancement observed at $\Delta = 0$, accompanied by two sideband amplifying peaks located at the same positions as in the linear output for $\kappa_2/\kappa_1 = -6$.

The amplitude of T and K exhibit significant sensitivity to the gain-to-loss ratio κ_2/κ_1. When $\kappa_2/\kappa_1 > 0$, the passive-passive system fails to achieve intracavity field localization, leading to a DIT profile in linear transmission and weak nonlinear output. The system remains in an unbroken $\mathcal{PT}$-symmetric phase within the range $-6 < \kappa_2/\kappa_1 < 0$. The gain in cavity B counters the losses in the system, ensuring its stability. By adjusting the ratio to traverse through the EP, both linear transmission and nonlinear output can be greatly enhanced. Upon $\kappa_2/\kappa_1 < -6$, the system transitions into the broken $\mathcal{PT}$-symmetric phase. In this phase, field intensity dynamically accumulates in cavity A due to strong field localization [49,51]. This accumulation effectively augments the nonlinear output intensity of the system.

2. *Coupled superconducting microwave resonators with artificial atoms*

The second physical system is constructed using superconducting circuits, employing two qubits to enable adjustable coupling interactions between atoms. When the coupling strength between the artificial atoms meets the condition $G \neq 0$, the first three terms of the field in resonator A can be obtained:

$$a_{II}^{(1)} = \frac{\epsilon_p\sqrt{\kappa_e}p_2}{p_1p_2 - p_3p_4}, \tag{22}$$

$$a_{II}^{(2)} = 0, \tag{23}$$

$$a_{II}^{(3)} = \frac{2ig(p_3 - p_2)(p_2 - p_4)}{\gamma(p_1p_2 - p_3p_4)^2}\left|\frac{\sqrt{\kappa_e}(p_2 - p_4)}{p_1p_2 - p_3p_4}\right|^2 \times \frac{\sqrt{\kappa_e}\epsilon_p|\epsilon_p|^2(ig + M_2G/2g)}{[\gamma/2 + i(\Delta + \delta + G)][\gamma^2/4 + (\Delta + \delta + G)^2]}, \tag{24}$$

in which $p_1 = (i\Delta + \kappa_1/2 + \kappa_e/2) + M_2$, $p_2 = (i\Delta + \kappa_b/2) + M_2$, $p_3 = Je^{i(\pi/2+\theta)} + M_2$, $p_4 = Je^{i(\pi/2-\theta)} + M_2$, and $M_2 = 2g^2/[\gamma/2 + i(\Delta + \delta + G)]$. Observations reveal that the nonzero terms of the field in resonator A can be altered by the value of G, potentially impacting the linear and nonlinear output of the system. Analogous to the first scenario, the two coefficients $\chi^{(1)}$ and $\chi^{(3)}$ can be computed.

In Fig. 4, the normalized linear transmission rate T and the third-order Kerr-nonlinear coefficient K are depicted for different coupling strengths between the two artificial atoms, illustrating their dependencies on the detuning Δ/κ_1

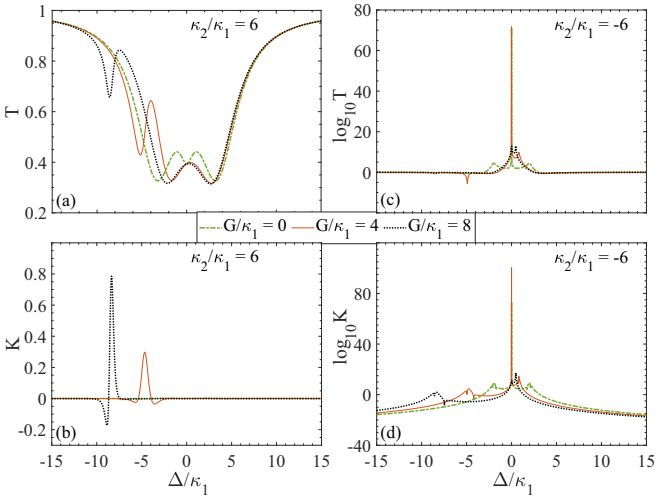

FIG. 4. The linear transmission rate T and Kerr-nonlinear coefficient K of the probe field vs the Δ/κ_1 for different coupling strengths G. When $\kappa_2/\kappa_1 = 6$, (a) the linear transmission rate T for $G = 0$ (green dash-dot line), $G = 4$ (red solid line), $G = 8$ (black dotted line). (b) Kerr-nonlinear coefficient K for the same values of G. For $\kappa_2/\kappa_1 = -6$, (c) the logarithm of T for the same values of G. (d) The logarithm of K for the same values of G. The remaining system parameters are defined as $J = 3\kappa_1$, $g = \kappa_1$, $\kappa_e = 5\kappa_1$, $\gamma = 0.7\kappa_1$, $\delta = 0$, and $\theta = \pi/2$.

in passive-passive or passive-active double-resonator configurations. For the scenario with $\kappa_2/\kappa_1 = 6$, Fig. 4(a) presents the linear transmission rate T as a function of Δ/κ_1. When $G = 0$, three absorption dips are observed, one at $\Delta = 0$ and the other two symmetrically positioned about it. As G increases, the symmetry of these curves is broken, and the absorption dip on the left side undergoes a noticeable blue shift. In Fig. 4(b), the nonlinear system output is displayed. Notably, for $G \neq 0$, the curves exhibit asymmetry about $\Delta = 0$ in contrast to the symmetric pattern observed at $G = 0$. This asymmetry can be elucidated by analyzing the system Hamiltonian (with $J = 0$, $\delta = 0$ and $\hbar = 1$):

$$\begin{aligned}\hat{H}_1 = {} & \Delta(\hat{a}^\dagger\hat{a} + \hat{b}^\dagger\hat{b}) + \Delta(\hat{\sigma}_1^+\hat{\sigma}_1^- + \hat{\sigma}_2^+\hat{\sigma}_2^-) \\ & + g[(\hat{a}^\dagger + \hat{b}^\dagger)(\hat{\sigma}_1^+ + \hat{\sigma}_2^+) + \text{H.c.}] \\ & + G(\hat{\sigma}_1^+\hat{\sigma}_2^- + \text{H.c.}) + \epsilon_p(\hat{a}^\dagger + \hat{a}).\end{aligned} \tag{25}$$

The spin interaction, expressed in symmetric and antisymmetric modes with resonance frequencies $\Delta \pm G$, can be reformulated as

$$\begin{aligned}\hat{H}_2 = {} & \Delta(\hat{a}^\dagger\hat{a} + \hat{b}^\dagger\hat{b}) + \epsilon_p(\hat{a}^\dagger + \hat{a}) \\ & + (\Delta + G)\hat{\sigma}_S^+\hat{\sigma}_S^- + (\Delta - G)\hat{\sigma}_A^+\hat{\sigma}_A^- \\ & + g[(\hat{a}^\dagger + \hat{b}^\dagger)\hat{\sigma}_S^+ + \text{H.c.}],\end{aligned} \tag{26}$$

in which $\hat{\sigma}_S^+ = (\hat{\sigma}_S^-)^\dagger \equiv (\hat{\sigma}_1^+ + \hat{\sigma}_2^+)/\sqrt{2}$ and $\hat{\sigma}_A^+ = (\hat{\sigma}_A^-)^\dagger \equiv (\hat{\sigma}_1^+ - \hat{\sigma}_2^+)/\sqrt{2}$. It is evident that the resonance between the cavities and qubits shifts from $\Delta = 0$ to the points $\Delta = \pm G$. The presence of only one resonant mode at $\Delta = -G$ is attributed to the coupling between the cavity and the symmetric mode (further insights can be found in Appendix B).

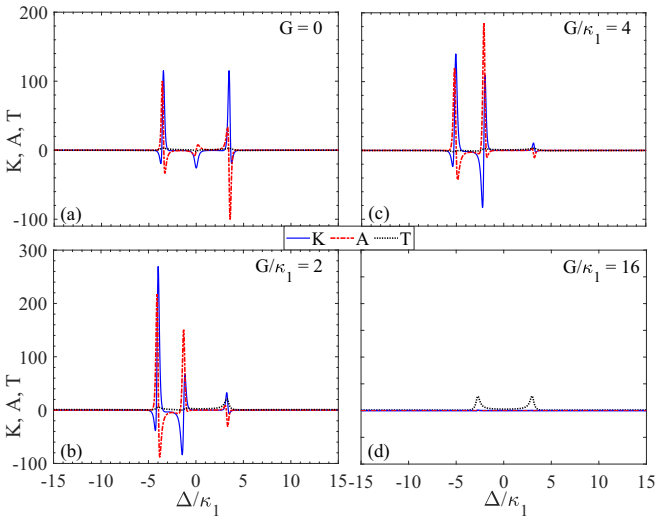

FIG. 5. The Kerr-nonlinear coefficient K (blue solid line), nonlinear absorption coefficient A (red dash-dot line), and linear transmission rate T (black dotted line) as functions of the detuning Δ/κ_1. (a) $G = 0$. (b) $G/\kappa_1 = 2$. (c) $G/\kappa_1 = 4$. (d) $G/\kappa_1 = 16$. The other parameters in the system are chosen as $\kappa_2 = -5\kappa_1$, $J = 4\kappa_1$, $g = \kappa_1$, $\kappa_e = 5\kappa_1$, $\gamma = 0.7\kappa_1$, $\delta = 0$, and $\theta = \pi/2$.

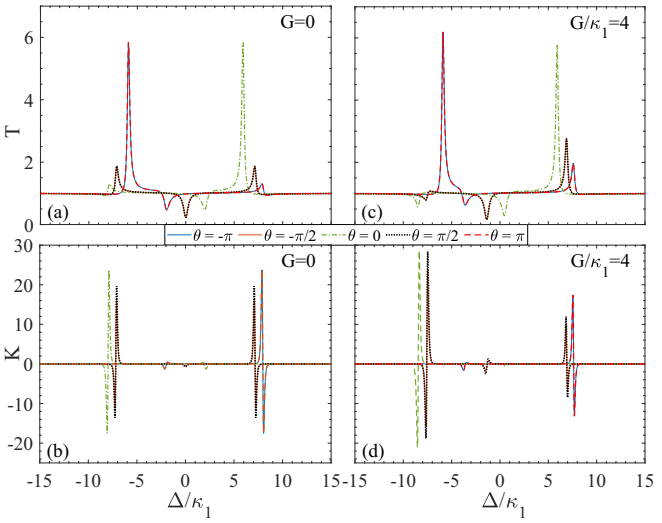

FIG. 6. The normalized linear transmission rate T and Kerr-nonlinear coefficient K of the probe field vs the detuning Δ/κ_1 for different values of the set $(G/\kappa_1, \theta)$. The blue solid, orange solid, green dash-dot, black dotted, and red dashed lines represent $\theta = -\pi$, $\theta = -\pi/2$, $\theta = 0$, $\theta = \pi/2$, and $\theta = \pi$, respectively. Other parameters include $g = 2\kappa_1$, $J = 6\kappa_1$, $\kappa_e = \kappa_1$, $\kappa_2 = -1.4\kappa_1$, $\gamma = 0.7\kappa_1$, and $\delta = 0$.

In the second scenario, where $\kappa_2/\kappa_1 = -6$, the logarithms of T and K are plotted as functions of Δ/κ_1 in Figs. 4(c) and 4(d), respectively. Analogous to the outcomes observed in the first physical system, when the gain-to-loss ratio satisfies $\kappa_2/\kappa_1 < 0$, both linear and nonlinear outputs witness substantial enhancements. At $G = 0$, the peaks of both linear and nonlinear outputs are located at $\Delta = 0$, accompanied by two sideband amplification peaks at $\Delta/\kappa_1 = \pm 2$. With an increase in G/κ_1 to 4, the maximum of T remains constant, while the maximum of K further escalates. The peak on the right shifts to approximately $\Delta/\kappa_1 = 0.8$ with heightened intensity, whereas the peak on the left shifts to $\Delta/\kappa_1 = -4.8$ with reduced intensity. When $G/\kappa_1 = 8$, the central peak at $\Delta = 0$ for both T and K drastically diminishes to roughly $T = 10^{13}$ and $K = 10^{11}$. The peak on the right intensifies to $T = 10^{13}$ and $K = 10^{17}$ at $\Delta/\kappa_1 = 0.5$, while the left peak weakens to $T = 0.25$ and $K = 87$ around $\Delta/\kappa_1 = -8.5$.

To contrast the field output at varying values of G, the Kerr-nonlinear coefficient K, nonlinear absorption A, and linear transmission T are depicted in Fig. 5 as functions of Δ/κ_1. Illustrated in Fig. 5(a), when $G = 0$, K exhibits an even symmetry with respect to Δ/κ_1, while A displays an odd function of Δ/κ_1. At the frequency corresponding to the right peak in K, T attains its maximum value, while A tends to zero. Subsequently, in Figs. 5(b)–5(d), for $G/\kappa_1 = 2, 4$, and 16, respectively, the interaction between the two artificial atoms disrupts the symmetry of all three curves. This phenomenon is likely attributed to the interference among three types of interactions: resonator-resonator, resonator-atom, and atom-atom couplings. This interference consequently influences the effective resonant modes within the system, akin to a quantum interference effect [85]. With an increase in G, the intensity of T remains relatively stable, while K and A initially rise and then decline. This amplification stems from the nonlinearity introduced by the two qubits. However, the decrease in the field output intensity could be a result of the competing interactions among these elements. A more robust coupling strength G than J and g may prioritize the atom-atom interaction over the resonator-resonator and resonator-atom interactions, causing energy confinement within the artificial atoms rather than emission from the system. The inclusion of G not only distorts the symmetry of the curves but also governs the peak value of the field output. This observation indicates that the intensity of the nonlinear output can be effectively modulated by the interactions of artificial atoms.

In Fig. 6, the normalized linear transmission rate T and Kerr-nonlinear coefficient K are plotted as functions of Δ/κ_1 for different values of the phase θ and coupling strength G. When $G = 0$, the plots of T and K against Δ/κ_1 are presented in Figs. 6(a) and 6(b). These two curves demonstrate symmetry about the $\Delta = 0$ axis when $\theta = \pm\pi/2$. With varying θ, the frequencies of the two peaks undergo certain shifts, where the amplitude of one peak can be magnified while the other is attenuated. The linear and nonlinear characteristics display contrasting variations with θ. For instance, at $\theta = 0$, T exhibits an intensified peak at $\Delta/\kappa_1 \approx 6$ and a diminished peak at $\Delta/\kappa_1 \approx -8$, while K features a heightened peak at $\Delta/\kappa_1 \approx -8$. Upon setting $\theta = \pm\pi$, T manifests a magnified peak at $\Delta/\kappa_1 \approx -6$ and a suppressed peak at $\Delta/\kappa_1 \approx 8$, whereas K displays a heightened peak at $\Delta/\kappa_1 \approx 8$. This attribute can be leveraged in scenarios necessitating enhanced nonlinearity alongside suppressed linear signals. In a distinct scenario where $G/\kappa_1 = 4$, Figs. 6(c) and 6(d) exhibit T and K as functions of Δ/κ_1. In contrast to the initial scenario, the curves lack symmetry, showcasing varied peak intensities and frequencies. The results underscore the capacity to tune the

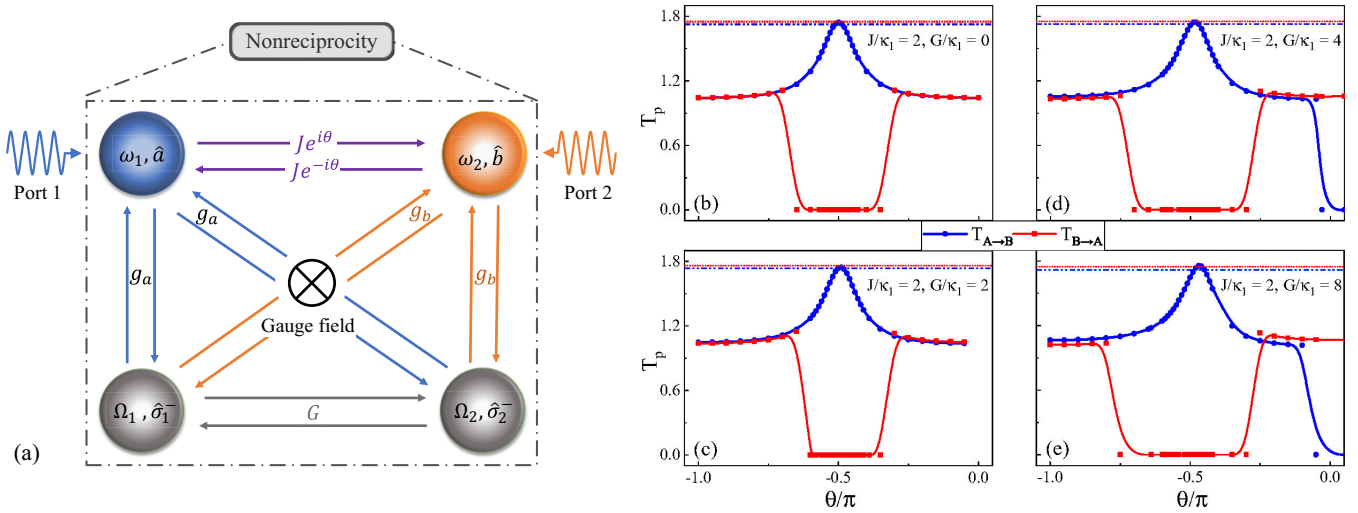

FIG. 7. Nonreciprocity in the $\mathcal{PT}$-symmetric system. (a) Schematic diagram of the system: Port 1 is for probe signal input to resonator A, while port 2 is for the signal driven on resonator B. The system features a phase-induced gauge field resulting from resonator-resonator coupling. Precise transmission results are calculated under system parameters: (b) $J/\kappa_1 = 2$, $G/\kappa_1 = 0$; (c) $J/\kappa_1 = 2$, $G/\kappa_1 = 2$; (d) $J/\kappa_1 = 2$, $G/\kappa_1 = 4$; and (e) $J/\kappa_1 = 2$, $G/\kappa_1 = 8$. The red circles and blue rectangles represent the transmission results when the input signal is applied to resonators A and B, respectively. The red dotted and blue dash-dot lines represent the transmission results when $J = 0$ and $G = 0$. The other parameters are $\kappa_2 = -3.6\kappa_1$, $g = \kappa_1$, $\kappa_e = 0.1\kappa_1$, $\gamma = 0.7\kappa_1$, and $\delta = 0$.

output field intensity and peak frequency of the passive-active double-resonator system by manipulating the parameter θ.

3. *Nonreciprocity of transmission*

As previously discussed, the linear transmission rate T and third-order Kerr-nonlinear coefficient K can be manipulated by several system parameters, including the gain-to-loss ratio κ_2/κ_1, resonator-resonator coupling strength J, atom-atom coupling strength G, and the phase θ embedded in J. To delve deeper into nonreciprocity, we independently stimulate both resonators and analyze the resultant transmission output. Here, the phase θ acts as the independent variable capable of altering the transmission output of the system. The numerical outcomes are derived from Eqs. (5)–(10):

$$\mathbf{H}_0 \begin{bmatrix} a \\ b \\ \sigma_1^z \\ \sigma_1^- \\ \sigma_2^z \\ \sigma_2^- \end{bmatrix} + \sqrt{\kappa_e} \begin{bmatrix} S_{\text{in}}^1 \\ S_{\text{in}}^2 \\ 0 \\ 0 \\ 0 \\ 0 \end{bmatrix} = 0. \tag{27}$$

When the probe field is applied to resonator A, the input signals are $S_{\text{in}}^1 = \epsilon_p$ and $S_{\text{in}}^2 = 0$. Similarly, when resonator B is excited, the input signals are $S_{\text{in}}^1 = 0$ and $S_{\text{in}}^2 = \epsilon_p$.

As illustrated in Fig. 7(a), two resonators, functioning as distinct ports, are stimulated by the probe field. According to Eq. (20), the transmission responses under two excitation directions are computed as $S_1 = 1 - a/\epsilon_p$ and $S_2 = 1 - b/\epsilon_p$. The modulated transmission output T_p influenced by the phase θ is plotted in Figs. 7(b)–7(e) for varying values of J and G. With the range from $-\pi$ to 0, the specific intervals of $T_{A\to B}$ and $T_{B\to A}$ span from -0.75π to -0.25π for $J/\kappa_1 = 2$ and $G/\kappa_1 = 0$, from -0.7π to -0.25π when $J/\kappa_1 = 2$ and $G/\kappa_1 = 2$, from -0.8π to -0.2π with $J/\kappa_1 = 2$ and $G/\kappa_1 = 4$, and from -0.85π to -0.2π for $J/\kappa_1 = 2$ and $G/\kappa_1 = 8$. The disparity between $T_{A\to B}$ and $T_{B\to A}$ signifies the nonreciprocity within the system. Evidently, one can tune the transmission output, irrespective of whether the input signal is directed towards resonator A or resonator B. This adaptability could be attributed to the gauge field introduced through the phase θ, which aids in breaking the time-reversal symmetry within the system [47,62,86]. Consequently, the transmission outcomes exhibit nonreciprocity along both propagation directions. Additionally, it appears that different values of J and G can alter the range of nonreciprocity. This phenomenon might offer a strategy for designing devices necessitating nonreciprocal transmission or potentially enabling unidirectional invisibility.

B. Properties of $\mathcal{PT}$ symmetry

The $\mathcal{PT}$-symmetric phase and $\mathcal{PT}$-broken phase are delineated through the linear and nonlinear output characteristics of the weak probe field. This section portrays the phase diagram of the first physical system by evaluating effective eigenvalues. By employing Eq. (4), the coefficient matrix can be expressed as follows:

$$H = \begin{bmatrix} \Delta - i\kappa_a/2 & Je^{i\theta} & g & g \\ Je^{-i\theta} & \Delta - i\kappa_b/2 & g & g \\ g & g & \zeta - i\gamma/2 & 0 \\ g & g & 0 & \zeta - i\gamma/2 \end{bmatrix}. \tag{28}$$

The qubit and the probe signal can be represented as $\zeta = \Delta + \delta$. To vividly illustrate distinct phases, the semiclassical Heisenberg-Langevin equations can be streamlined based

on the steady-state approximation ($d\sigma_1^z/dt = d\sigma_1^-/dt = d\sigma_2^z/dt = d\sigma_2^-/dt = 0$) [87]:

$$\frac{da}{dt} = -\left(i\Delta + \frac{\kappa_a}{2}\right)a - Je^{i(\frac{\pi}{2}+\theta)}b - M + \epsilon_p\sqrt{\kappa_e}, \quad (29)$$

$$\frac{db}{dt} = -\left(i\Delta + \frac{\kappa_b}{2}\right)b - Je^{i(\frac{\pi}{2}-\theta)}a - M, \quad (30)$$

in which

$$M = \frac{M_1\gamma(a+b)}{\gamma + (M_1 + M_1^\star)|a+b|^2}, \quad (31)$$

and $M_1 = 2g^2/[\gamma/2 + i(\Delta+\delta)]$. Then, the matrix form is

$$H = \begin{bmatrix} \Delta - i\kappa_a/2 - iM & Je^{i\theta} - iM \\ Je^{-i\theta} - iM & \Delta - i\kappa_b/2 - iM \end{bmatrix}. \quad (32)$$

The eigenvalues are

$$\lambda_\pm = \left[\Delta - \frac{i}{4}(\kappa_a + \kappa_b + 4M)\right] \pm \sqrt{J^2 - M^2 - 2iMJ\cos\theta - \frac{1}{16}(\kappa_a - \kappa_b)^2}. \quad (33)$$

It can be observed that when $\kappa_b/\kappa_a < 0$, the unbroken $\mathcal{PT}$-symmetric phase fulfills the condition $J^2 - M^2 - 2iMJ\cos\theta - \frac{1}{16}(\kappa_a - \kappa_b)^2 > 0$. Conversely, the broken $\mathcal{PT}$-symmetric phase occurs in the range satisfying $J^2 - M^2 - 2iMJ\cos\theta - \frac{1}{16}(\kappa_a - \kappa_b)^2 < 0$.

The phase diagram of the $\mathcal{PT}$-symmetric system is illustrated in Fig. 8(a) showing the real (solid lines) and imaginary parts (dashed lines). The system can transition between the broken $\mathcal{PT}$-symmetric phase and the unbroken $\mathcal{PT}$-symmetric phase by adjusting the gain-to-loss ratio. Three distinct regimes are outlined: (1) $\kappa_2/\kappa_1 > 0$, corresponding to the non-$\mathcal{PT}$-symmetric regime; (2) $-6 < \kappa_2/\kappa_1 < 0$, representing the unbroken $\mathcal{PT}$-symmetric regime; and (3) $\kappa_2/\kappa_1 < -6$, indicating the broken $\mathcal{PT}$-symmetric regime. During the phase of (1), the system behaves akin to a passive-passive system without output field enhancement. In the phase of (2), nonzero imaginary parts in the eigenvalues are attributed to the dominant photon-tunneling effects, characterized by J and θ, surpassing the intracavity localization effects associated with the gain-to-loss ratio. This suggests that the gain in resonator B fails to offset the overall loss in the system [45]. It is possible to adjust $Je^{i\theta}$ or κ_2/κ_1 to induce a $\mathcal{PT}$ transition within the system. Phase (3) is marked by an escalation in the field intensity within resonator A, consequently amplifying the nonlinear output of the system. At $\kappa_2/\kappa_1 \approx -6$, this aligns with the EP of the $\mathcal{PT}$ transition in the passive-active double-resonator system. Near the EP, a significant boost in the output field is anticipated [49,51]. The logarithm of the maximum linear transmission rate $T_{\max}$ and the maximum third-order Kerr-nonlinear coefficient $K_{\max}$ are plotted as functions of the gain-to-loss ratio κ_2/κ_1 in Figs. 8(b) and 8(c), correspondingly. Both parameters indicate a conspicuous enhancement when the ratio κ_2/κ_1 approximates the EP value. The values of $T_{\max}$ and $K_{\max}$ are computed using Eqs. (20) and (21) derived from the semiclassical Heisenberg-Langevin equations of motion, while the phase diagram is formulated from Eq. (32) with estimates from Eqs. (29) and (30). The EPs in these figures are nearly identical, signifying strong concurrence between the results obtained via the perturbation approach and the steady-state approximation.

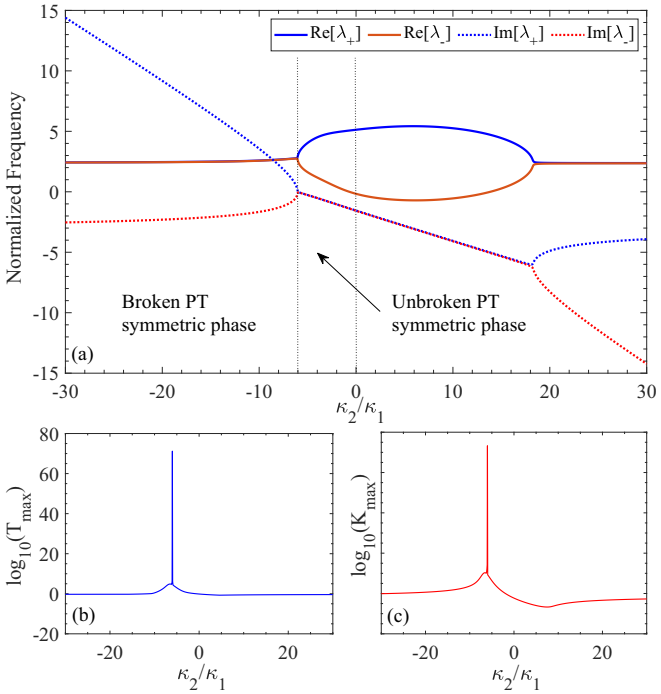

FIG. 8. The phase diagram of the $\mathcal{PT}$-symmetric system and enhancement of linear and nonlinear properties by breaking $\mathcal{PT}$ symmetry. (a) The phase diagram of the system. The real and imaginary parts of the effective eigenfrequencies $\lambda_\pm$ of this system are plotted as functions of the gain-to-loss ratio κ_2/κ_1. Blue solid and dashed lines are the real and imaginary parts of λ_+, while red solid and dashed lines are the real and imaginary parts of λ_-. (b) The logarithm of the maximum linear transmission T as a function of the gain-to-loss ratio κ_2/κ_1. (c) The logarithm of the maximum third-order Kerr-nonlinear coefficient K as a function of the ratio κ_2/κ_1. The other parameters are chosen as $g = \kappa_1, J = 3\kappa_1, \kappa_e = 5\kappa_1$, $\gamma = 0.7\kappa_1, \delta = 0$, and $\theta = \pi/2$.

C. Modulation of $\mathcal{PT}$ symmetry

The phase diagram of the $\mathcal{PT}$-symmetric system has been computed, illustrating the amplification of both linear and nonlinear outputs to delineate the EP of the phase transition. It has been demonstrated that by adjusting the gain-to-loss ratio κ_2/κ_1, the phase within the system can be controlled, with an EP corresponding to a specific value of κ_2/κ_1 given particular system parameters. This section investigates various parameters in the system, such as the phase θ and the coupling strengths J and G, to modulate the EP of the phase transition.

The energy-level arrangement of the system is shown in Fig. 9(a), showcasing two resonators and two artificial atoms engaging in interactions that can result in energy-level splittings within the system. Subsequently, Figs. 9(b)–9(d) examine three system parameters, the phase θ and the coupling strengths J and G, to manipulate the EP of the phase transition. To begin, in Fig. 9(b), the influence of the phase

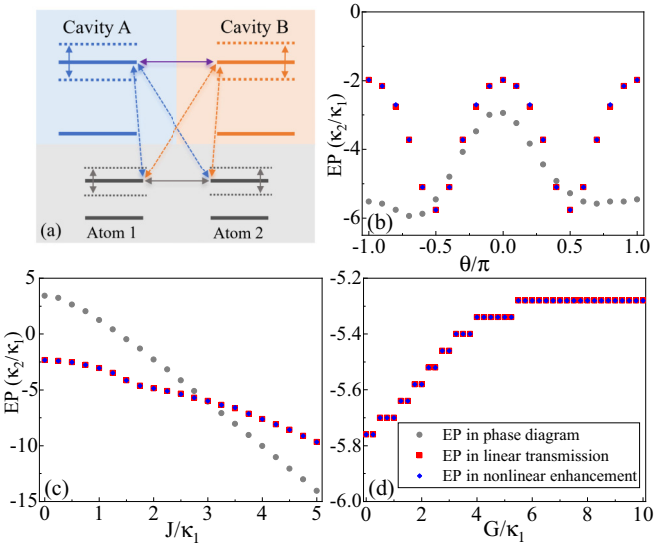

FIG. 9. Modulation of EP of the $\mathcal{PT}$ phase transition. (a) The energy-level configuration of the system consists of two resonators and two artificial atoms. Three parameters, namely, (b) the phase θ, (c) the coupling strength J, and (d) the coupling strength G, have been investigated to modulate the EP of the phase transition, which is determined by κ_2/κ_1 in the system. Gray circles, red rectangles, and blue rhombuses represent the EPs estimated from the phase diagram, the maximum point in linear transmission, and the maximum point in nonlinear enhancement, respectively.

θ on modulating the EP is illustrated. It is observed that adjustments in the phase can induce periodic fluctuations in the EP value. The EP derived from the phase diagram demonstrates a correlation with the trends seen in both linear and nonlinear enhancements, although divergences exist due to varying approximation methodologies. At $\theta = \pm\pi/2$, the EP ratio value is approximately -6, consistent with the findings in Sec. III C. Conversely, at $\theta = \pm\pi$ or zero, the ratio hovers around -2. Next, in Fig. 9(c), the effect of the coupling strength J on modulating the EP is investigated. In this analysis, it is observed that the EP determined from the phase diagram deviates significantly from the EP obtained through linear and nonlinear enhancements. However, both methodologies converge on an EP value of $\kappa_2/\kappa_1 = -6$ when $J/\kappa_1 = 3$. The results of output field enhancement indicate that the EP value ranges from -2.5 to -10 as J/κ_1 varies from 0 to 5. In Fig. 9(d), the impact of the coupling strength G on modulating the EP is demonstrated. In this instance, the interaction between two qubits is considered a perturbation to the system for simplicity. It has been verified that the EP values, estimated from the peak points in both linear and nonlinear outputs, increase with larger G. Specifically, the EP value transitions from -5.8 to -5.3 as G/κ_1 ranges from 0 to 10. This observation suggests that intensified interactions between the two artificial atoms may result in a higher EP value associated with the gain-to-loss ratio. These system parameters serve as effective tools for adjusting the exceptional point of the $\mathcal{PT}$-symmetric phase transition, thus enhancing the versatility of the system to a certain degree. For further details, please consult the second section of Appendix A.

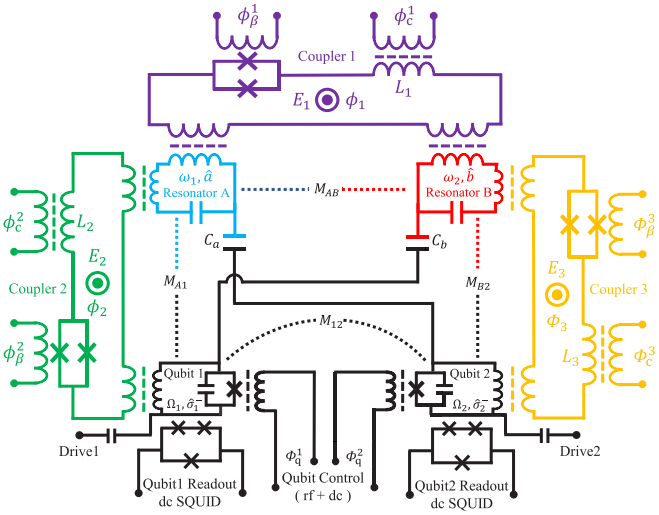

FIG. 10. Circuit diagram for the phase qubit (black), resonator (blue and red), and couplers between resonators (purple) and between qubit and resonator (in green and orange).

IV. EXPERIMENTAL SETUP

In this section, we aim to provide a succinct discussion on the experimental implementation based on existing experimental techniques. As displayed in Fig. 10, one feasible setup for this study involves two phase qubits [88] equipped with geometric inductance, capacitance, and Josephson junctions, along with two resonators featuring geometric inductance and capacitance. The phase qubits are regulated by a single flux-bias line supplying dc and rf flux ϕ_q^i, $(i = 1, 2)$. Qubit readout is realized through a short pulse that induces tunneling of the excited state. The system further includes three tunable couplers achieved using an rf SQUID loop with geometric inductance and two junctions, forming a dc SQUID to alter the properties of the rf SQUID [89–92]. The couplers are controlled by two external flux-bias lines: one imposing flux ϕ_c^j on the rf SQUID and the other applying flux ϕ_β^j to the embedded dc SQUID via inductance L_j, $(j = 1, 2, 3)$. Based on these couplers, effective mutual inductances such as M_{AB}, M_{A1}, M_{B2}, and M_{12} among them are defined. Resonators A and B are coupled to qubits 2 and 1 via C_a and C_b, respectively. It is important to note that the circuit design could alternatively incorporate other superconducting qubits.

For the phase in a gauge field, it can manifest in any coupling arrangement between qubits or resonators. Firstly, there is ϕ_1 established between two resonators. Secondly, there are ϕ_2 and ϕ_3 existing between a resonator and a qubit. Lastly, there is a phase interaction between two phase qubits. For simplicity, the phase involvement in the coupling between two resonators is illustrated as a representative case (highlighted in purple in Fig. 10), while the other coupling scenarios are all grounded in geometric capacitance. The collective flux bias administered to the coupler can be expressed as [92]

$$\phi_1 = \phi_1^0 + \delta\phi_1 \cos(f_1\tau + \theta_1), \tag{34}$$

in which the first term ϕ_1^0 represents the dc magnetic flux, and the second term signifies the ac magnetic flux at frequency f_1 and initial phase θ_1. Then, the current flowing through this

TABLE I. Experimental observations of qubit-resonator and qubit-qubit coupling in superconducting quantum circuits.

Reference	Qubit type [a]	Cavity type [b]	$\gamma/2\pi$ [c](MHz)	$\kappa/2\pi$ [d](MHz)	$g/2\pi$ [e](MHz)	$\omega_r/2\pi$ [f](GHz)	Notes
Allman *et al.* (2010) [89]	PQ	LE	7.4	1	q-r: 0–100	7.71	Coherent tunable coupling
Allman *et al.* (2014) [90]	PQ	LE	1.1	0.6	q-r: 0.4–482	7.2	Enable to introduce phase in the coupler
Yoshihara *et al.* (2018) [93]	FQ	LE	∼1	∼1	q-r: 7480	6.335	Deep-strong-coupling regime
Yoshihara *et al.* (2017) [94]	FQ	LE	∼1	∼1	q-r: 7630	5.711	First DSC work
Hoi *et al.* (2011) [95]	TQ	TL	73–96	—	—	—	Single photon router
Noh *et al.* (2023) [96]	TQ	LE	0.135	10	q-r: 10	9.4	Statically decoupled qubits from the cavity
Stehlik *et al.* (2021) [97]	TQ	—	9-562	—	q-r: 80, 110 q-q: 6	—	Fixed frequency of qubits with tunable coupling
Xu *et al.* (2020) [98]	XQ	LE	—	—	q-r: 122 q-q: 12	6.74 (c)	CZ-gate with fidelity 99.5%
Kandala *et al.* (2021) [99]	TQ	LE	0.0087	—	q-r: 87.5, 88.5 q-q: 6.2	5.964	Multi paths coupling

[a]PQ: phase qubit; FQ: flux qubit; TQ: transmon qubit; XQ: Xmon qubit.
[b]LE: lumped-element resonator; TL: transmission line resonator.
[c]γ: qubit decay rate.
[d]κ: photon decay rate.
[e]g: coupling strength; q-r: qubit-resonator coupling; q-q: qubit-qubit coupling.
[f]ω_r: resonator frequency; c: coupler frequency.

coupler is

$$I_1 = I_1^0 \sin\left[\frac{2\pi}{\Phi_0}(\phi_1 - L_1 I_1)\right], \tag{35}$$

in which I_1^0 denotes the critical current of the Josephson junction in the coupler, and $\Phi_0 = h/2e$ is the magnetic flux quantum. With these definitions, the effective mutual inductance established by coupler 1 ($M_1 = M_{AB}$) would satisfy

$$\begin{aligned} M_1^{\text{eff}} &= M_1^2 \frac{\partial I_1}{\partial \phi_1} \\ &= \frac{M_1^2}{L_1} \frac{\alpha_1 \cos[2\pi(\phi_1 - L_1 I_1)/\Phi_0]}{1 + \alpha_1 \cos[2\pi(\phi_1 - L_1 I_1)/\Phi_0]}, \end{aligned} \tag{36}$$

in which $\alpha_1 = 2\pi I_1^0 L_1/\Phi_0$. Applying the weak ac flux bias condition, which is $\delta\phi_1 \ll \phi_1^0$, the effective mutual inductance can be transformed by a Taylor-series centered at ϕ_1^0:

$$M_1^{\text{eff}} = \sum_{r=0}^{\infty} \frac{1}{r!} \frac{\partial^r M_1^{\text{eff}}}{\partial(\phi_1)^r}|_{\phi_1=\phi_1^0} \left(\phi_1 - \phi_1^0\right)^r. \tag{37}$$

In this situation, it can be truncated to the first-order term of the parameter $\delta\phi_1$. Then, the mutual inductance is approximately calculated as

$$M_1^{\text{eff}} \approx M_1^0 + \delta M_1 \cos(f_1 \tau + \theta_1), \tag{38}$$

in which these terms satisfy

$$\begin{aligned} M_1^0 &= \frac{M_1^2}{L_1} \frac{\alpha_1 \cos\beta_1}{1 + \alpha_1 \cos\beta_1}, \\ \delta M_1 &= -\frac{M_1^2}{L_1} \frac{2\pi\alpha_1 \sin\beta_1}{[1 + \alpha_1 \cos\beta_1]^3} \frac{\delta\phi_1}{\phi_0}, \\ \beta_1 &= \frac{2\pi\left(\phi_1^0 - L_1 I_1|_{\phi_1=\phi_1^0}\right)}{\Phi_0}. \end{aligned} \tag{39}$$

Based on coupler 1, the coupling strength between resonators can be tuned, and the coupling phase can be adjusted by varying the external flux signal. Recent experimental findings [100,101] confirm the feasibility of meeting all the aforementioned conditions. To enhance the transparency of these parameters, we present a selection of pertinent experiments in Table I, detailing circuit designs, the range of coupling strength, and the accomplishment of adjustable phase within the circuit. Based on these references, it appears straightforward to modulate the phase within a system featuring multiple coupling paths. Furthermore, ongoing experimental advancements hold the promise of refining the characteristics of these systems in the near term, thereby significantly increasing the prospects of achieving heightened controllability.

V. CONCLUSIONS

The superconducting circuit presents significant advantages in scalability and adjustability, holding great promise for realizing the model discussed in this study. A comparison with systems constructed using microcavities and atoms reveals that incorporating controllable qubit-qubit coupling profoundly affects both the linear and nonlinear system outputs. The phase disparity between the two resonators correlates with the nontrivial gauge phase encompassing the entire system, exerting influence on both the symmetry and magnitude of the transmission output. By individually introducing the probe signal into each resonator, the modulation of phase can induce nonreciprocity in transmission. By adjusting the gain-to-loss ratio κ_2/κ_1, we have observed and validated a phase transition in the $\mathcal{PT}$-like-symmetric system through the phase diagram. Proximity to the exceptional point in the phase diagram showcases an intensified field output, providing a foundation for signal amplification with feeble input fields. To bolster the adaptability of the system, parameters such as phase θ and coupling strengths J and G have exhibited the capability to modulate the EP of the phase transition. It has been observed that the interaction between artificial atoms can, to some extent, enhance nonlinear output and provide a means to modulate phase transitions within the system. With these advancements, we anticipate that experimental investigations on chip-scale superconducting circuits utilizing $\mathcal{PT}$-like-symmetric systems possess the potential to facilitate additional applications in on-chip signal modulation, quantum information processing, and the establishment of large-scale quantum networks.

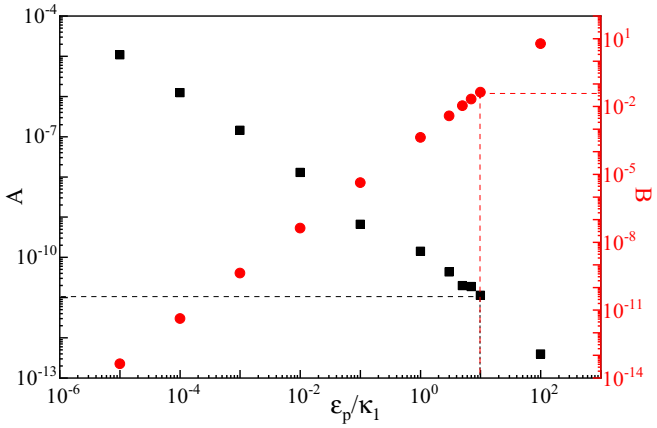

FIG. 11. Fluctuations A and B vs driven signal ϵ_p. The other parameters in the system are chosen as $g = \kappa_1$, $J = 2\kappa_1$, $\kappa_e = 5\kappa_1$, $\gamma = 6\kappa_1$, $\Delta = 0$, $\delta = 2\kappa_1$, $\kappa_2 = 3.6\kappa_1$, and $\theta = \pi/2$.

ACKNOWLEDGMENTS

This work is supported by the National Key Research and Development Program of China under Grant No. 04400100122. We thank Yunqiu Ge for valuable discussions.

APPENDIX A: APPROXIMATION METHODS

1. Steady-state approximation and weak excitation approximation

In this Appendix, we analyze the appropriate range of the probe signal ϵ_p to ensure the validity of the two approximation methods applied in Eqs. (5)–(14), namely, the steady-state and weak excitation approximations. To enhance the accuracy of our findings, we employ the numerical method offered by the ode113 function in MATLAB. The fluctuation of the annihilation operator of cavity 1, denoted as $\langle a\rangle$, is defined as

$$A = \frac{\langle a\rangle_{\max} - \langle a\rangle_{\min}}{\langle a\rangle_{\text{ave}}}, \tag{A1}$$

and the fluctuation of Pauli operator of qubit 1 $\langle\sigma_1^z\rangle$ is

$$B = \frac{\left[\left(\langle\sigma_1^z\rangle_{\max} - 0.5\right)^2 + \left(0.5 - \langle\sigma_1^z\rangle_{\min}\right)^2\right]^{1/2}}{\langle\sigma_1^z\rangle_{\text{ave}}}. \tag{A2}$$

The values of A and B tuned by the ratio ϵ_p/κ_1 are displayed in Fig. 11. It can be seen that as the ratio ϵ_p/κ_1 varies from 10^{-5} to 10^2, the value of A decreases from 10^{-5} to 10^{-13} as a result of the increase in $\langle a\rangle$, whereas the value of B escalates from 10^{-14} to 10. At $\epsilon_p/\kappa_1 = 10$, the approximate values of A and B are achieved at 10^{-10} and 10^{-2}, respectively. In accordance with various pertinent experiments [102–104], the intensity of the driving signal can be adjusted as needed. Consequently, if the ratio $\epsilon_p/\kappa_1 \leqslant 10$ holds, both approximation methods remain valid, and the experimental configuration is deemed feasible. Additionally, the specific value of ϵ_p/κ_1 does not influence the outcomes detailed in the main text, as the driving signal power has been normalized according to Eqs. (20) and (21). All other parameters applied in this work have been thoroughly scrutinized for feasibility and validity [105–108].

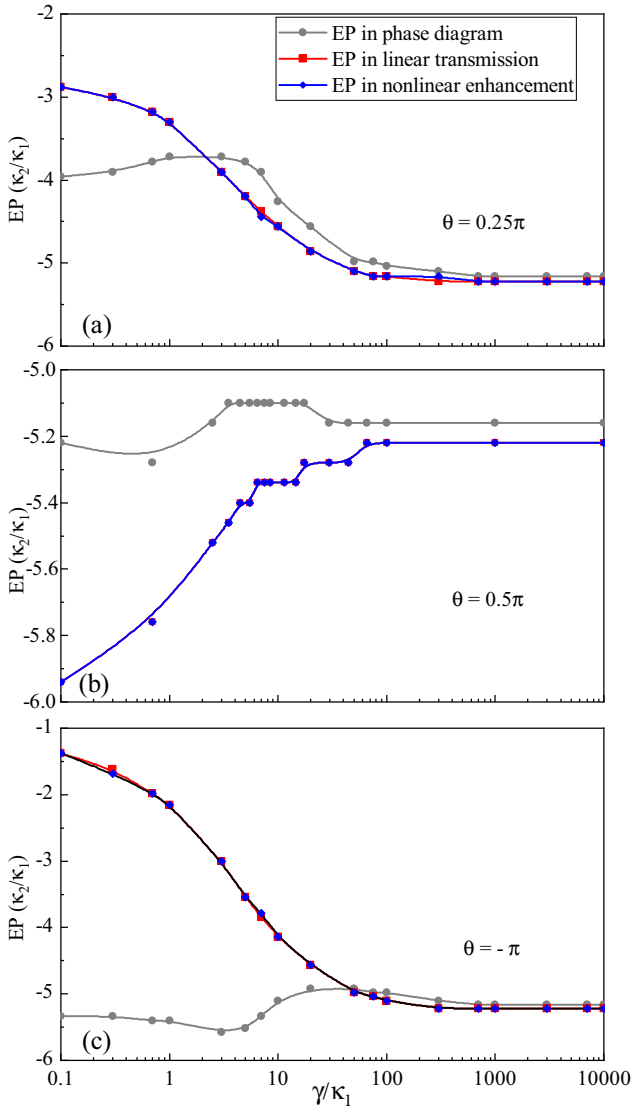

FIG. 12. Schematic depiction of EP (κ_2/κ_1) modulated by the decay rate of qubits γ/κ_1. (a) The phase is $\theta = 0.25\pi$. (b) The phase is $\theta = 0.5\pi$. (c) The phase is $\theta = -\pi$. The other parameters in the system are chosen as $g = \kappa_1$, $J = 2.8\kappa_1$, $\kappa_e = 5\kappa_1$, $\Delta = 3\kappa_1$, $\delta = 0$, and $\epsilon_p = \kappa_1$.

2. Transformation from four-body to effective two-body system

In this section, our focus lies on transitioning the system from a cavity-qubit system to one comprising two effective cavities. As mentioned in the main text, we presuppose the qubit to be in a steady state, which means that the decay rate of the qubit γ plays a crucial role in this transformation, altering the value of the exceptional point. Consequently, we delve into exploring the influence of γ on the approximation of the exceptional point during the phase transition. The schematic depiction of EP modulation by the decay rate of qubits under different coupling phases is shown in Fig. 12. The coupling phases illustrated are (a) 0.25π, (b) 0.5π, and (c) $-\pi$. It is evident that with an increasing γ/κ_1, the EP values calculated by both methods tend to converge. At the theoretical limit, both methods yield the same EP value, as the modulation of θ on the phase transition diminishes when

$\gamma/\kappa_1 \to \infty$. This convergence arises from the reduced impact of the qubit on the cavity due to excessive dissipation, disrupting the quantum interference engendered by multiple paths. This situation resembles the "bad cavity limit" [109–112]. In practical applications, achieving an infinitesimal difference in EP calculation is unattainable, as we cannot realize qubits with infinite dissipation. Furthermore, the decay rate must be constrained for an effective $\mathcal{PT}$ system to ensure phase transition modulation stability and functionality. In Fig. 12 of the main text, a specific parameter set chosen can lead to noticeable disparities in the results between the two methods; however, overall, they exhibit similar trends in their curves.

The discrepancies observed in the EP calculations using both methods can be ascribed to the approximation techniques employed during the model transformation process. In fact, the model derived from Eqs. (29) and (30) overlooks certain dynamics of the overall system outlined in Eqs. (5)–(10). For instance, the assumption that the behavior of the two qubits can be represented by two effective cavities implies a system in a steady state. The rationale behind employing this transformation to elucidate the $\mathcal{PT}$ phase transition lies in the mixed nature of the coefficient matrix in Eq. (28), encompassing both cavity and qubit components. While the former exhibits Boson-like characteristics, the latter embodies Fermion-like attributes, introducing a conflict. Our objective is to represent the two emitters equivalently within a model constructed using two effective cavities to derive analytical eigenvalues from the coefficient matrix. This strategy enables us to establish a clear correlation between phase transition points and diverse parameters, facilitating discussions on the modulation of phase transition points.

APPENDIX B: PROPERTIES OF PURE CAVITY SYSTEM

In this Appendix, a system consisting of four linear cavities is constructed to elucidate particular phenomena observed in cavity-qubit systems. To investigate the origin of asymmetry in the cavity-qubit system, the intercavity coupling within the cavity system is configured akin to the cavity-qubit model. For simplicity, all four cavities are resonant, possess identical decay rates, and exhibit uniform coupling strengths defined as g. As shown in Fig. 13, three scenarios are examined: (1) absence of direct coupling between cavities 1 and 3, (2) presence of direct coupling between cavities 1 and 3, and (3) inclusion of direct coupling among cavities 1 and 3, as well as 2 and 4, to analyze the transmission outcomes.

The semiclassical Heisenberg-Langevin equations of the system can be written as

$$\frac{dm}{dt} = -\left(i\Delta + \frac{\kappa}{2}\right)m - ig(n+p+q) + \epsilon_p\sqrt{\kappa_e}, \tag{B1}$$

$$\frac{dn}{dt} = -\left(i\Delta + \frac{\kappa}{2}\right)n - ig(m+p+q), \tag{B2}$$

$$\frac{dp}{dt} = -\left(i\Delta + \frac{\kappa}{2}\right)p - ig(m+n+q), \tag{B3}$$

$$\frac{dq}{dt} = -\left(i\Delta + \frac{\kappa}{2}\right)q - ig(m+n+p). \tag{B4}$$

The linear transmission would be calculated as described in the main text. Here, we utilize the coefficient matrix of the system to calculate the intercoupling among the system for the three cases.

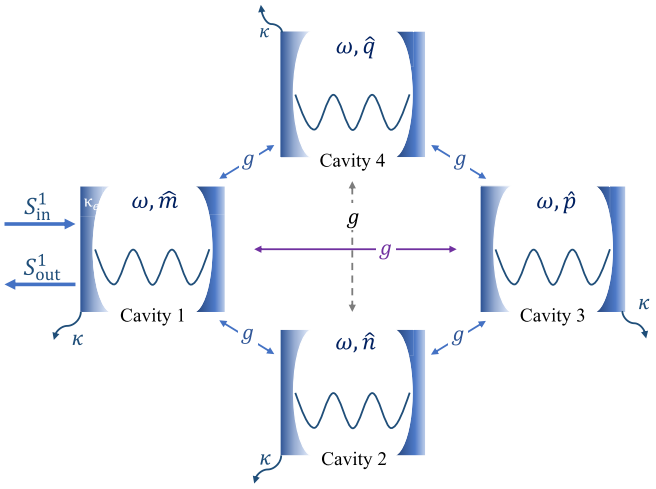

FIG. 13. Schematic depiction of a system constructed by four cavities.

For the first case, the matrix is

$$H_{\mathrm{I}} = \begin{bmatrix} \Delta - i\kappa/2 & g & 0 & 0 \\ g & \Delta - i\kappa/2 & g & 0 \\ 0 & g & \Delta - i\kappa/2 & g \\ g & 0 & g & \Delta - i\kappa/2 \end{bmatrix}. \tag{B5}$$

The system has three resonant modes Δ, $\Delta - 2g$, and $\Delta + 2g$, which are symmetrical about the axis $\Delta = 0$. There is only one route for information transfer, and the four cavities can be treated as identical due to the highly symmetric structure.

For the second case, the matrix would be

$$H_{\mathrm{II}} = \begin{bmatrix} \Delta - i\kappa/2 & g & g & g \\ g & \Delta - i\kappa/2 & g & 0 \\ g & g & \Delta - i\kappa/2 & g \\ g & 0 & g & \Delta - i\kappa/2 \end{bmatrix}, \tag{B6}$$

having four resonant modes Δ, $\Delta - g$, $\Delta + (\frac{1}{2} - \frac{\sqrt{17}}{2})g$, and $\Delta + (\frac{1}{2} + \frac{\sqrt{17}}{2})g$, which are asymmetric about the axis $\Delta = 0$. This asymmetry stems from broken symmetry and quantum interference engendered by multiple pathways. As shown in Fig. 14(a), the introduction of coupling interaction between cavities 1 and 3 delineates a distinction between these cavities and cavities 2 and 4, signifying a break in system symmetry. Upon inputting a probe signal into cavity 1, it can traverse through the system via diverse pathways, noted in distinct

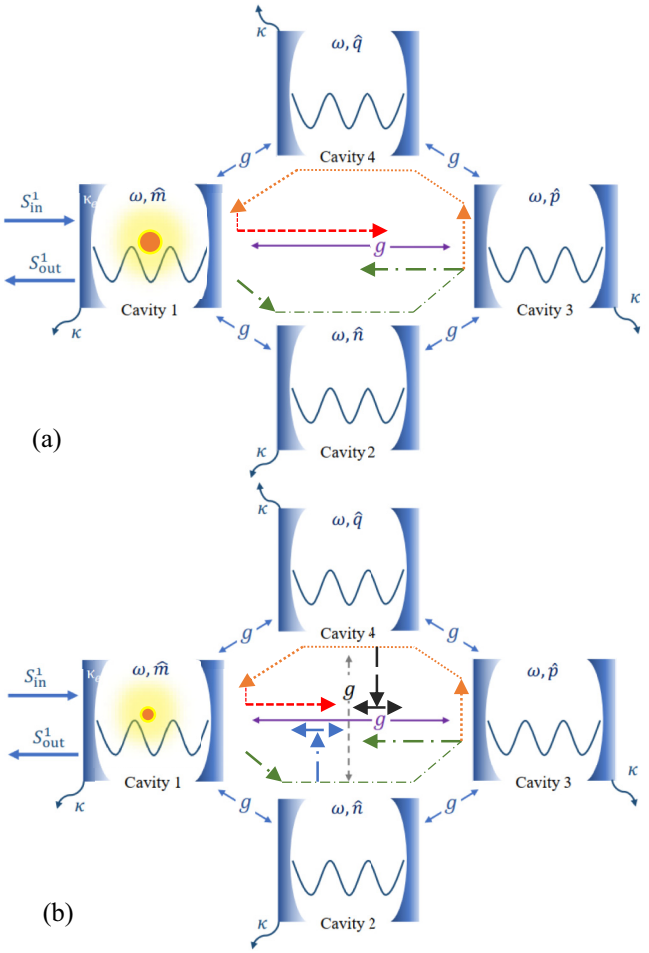

FIG. 14. Information transfer among the four cavities. (a) Direct coupling between cavities 1 and 3. (b) Direct coupling between cavities 1 and 3, as well as cavities 2 and 4.

colors. These pathways interact, causing a modulation of effective mode frequencies within the system. Consequently, owing to broken symmetry and quantum interference induced by multiple pathways, the output of the system exhibits a marked deviation from its previous state, manifesting asymmetry.

As for the third case, the matrix is

$$H_{\mathrm{III}} = \begin{bmatrix} \Delta - i\kappa/2 & g & g & g \\ g & \Delta - i\kappa/2 & g & g \\ g & g & \Delta - i\kappa/2 & g \\ g & g & g & \Delta - i\kappa/2 \end{bmatrix}. \tag{B7}$$

The system has two resonant modes, $\Delta - g$ and $\Delta + 3g$, asymmetric around the axis $\Delta = 0$. This asymmetry can be attributed to quantum interference. As Fig. 14(b) demonstrates, the information transfer propagation is notably more intricate compared to the preceding scenario. While the added coupling between cavities 2 and 4 enhances the propagation complexity, it aids in restoring the high symmetry of the system. Consequently, these four modes degenerate into two, with one mode transitioning to $\Delta - g$ and the other to $\Delta + 3g$.

In the cavity-qubit $\mathcal{PT}$-symmetric system, the presence of qubit nonlinearity and gain within a single component distinguishes it from a pure cavity system. Initially, there is no direct interaction between atoms or cavities ($G = 0, J = 0$). As shown in Fig. 2(a), three resonant modes are observed, resembling the phenomenon in the initial case of the pure cavity system. This similarity arises from both systems having only one route for information transfer, devoid of any competition or interference. In Fig. 4(b), cavity 2 exhibits a positive value rather than a negative one, with the disparities attributed to the presence of gain within the system. In the next scenario, there exists direct interaction between cavities ($G = 0, J \neq 0$). As shown in Fig. 2(a), the transmission curve exhibits symmetry, and resonant modes remain intact. This behavior contrasts with the asymmetry observed in the second case of the pure cavity system, where $J \neq 0$ induces no asymmetry in the cavity-qubit system. Compared with the first case, cavity mode (boson) is unidentical with qubit (fermion), therefore the additional coupling route between cavities does not disrupt the symmetry of the original system. Moreover, the cavity-qubit coupling, distinct from cavity-cavity coupling, may introduce significant quantum interference effects within a system featuring multiple pathways. Consequently, the value of J can modulate the frequencies of resonant modes rather than the symmetry of transmission curves. In the third scenario, there is direct interaction between cavities and atoms ($G \neq 0, J \neq 0$). As evident from Fig. 4(a), the curves display asymmetry, featuring three distinct resonant modes. Comparative analysis with the third case of the pure cavity system indicates that the frequencies and symmetries of two resonant modes situated away from the $\Delta = 0$ axis are primarily influenced by quantum interference, while the single mode adjusted by the coupling strength G is linked with qubit properties. In Fig. 4(c), the observed differences can be attributed to the gain in cavity 2. A notable observation is the emergence of a different mode at $\Delta = 0$ in the positive-negative system. With an increase in qubit-qubit coupling strength G, there is a tendency for the intensity of the right mode to increase and that of the left mode to decrease. This phenomenon may be linked to quantum interference within the system. Moreover, it appears that the left mode synchronously changes with G, indicating a possible influence of qubit-qubit coupling on it. Regarding the physical origin of nonlinear output, the first case occurs when $G = 0$ and $J \neq 0$, while the second case emerges when $G \neq 0$ and $J \neq 0$. It can be observed that qubit-qubit coupling can augment the intensity of nonlinear output when cavity 2 is negative. In Fig. 4(d), with cavity 2 being positive, the introduction of qubit coupling disrupts the symmetry of the nonlinear output curves. This phenomenon may be akin to the disruption observed in linear transmission: the appearance of the resonant mode at $\Delta = 0$ is predominantly due to the $\mathcal{PT}$-symmetric system, while the modulation of the sideband modes is influenced by quantum interference and qubit interactions. It is inferred from Eq. (24) in the main text that the numerator $M_2 G/2g$ signifies the substantial impact of G on the nonlinear output of the system.

[1] J. V. Selinger, Director deformations, geometric frustration, and modulated phases in liquid crystals, Annu. Rev. Condens. Matter Phys. **13**, 49 (2022).

[2] A. M. Shaltout, V. M. Shalaev, and M. L. Brongersma, Spatiotemporal light control with active metasurfaces, Science **364**, eaat3100 (2019).

[3] G. Moon, M. S. Heo, Y. Kim, H. R. Noh, and W. Jhe, Nonlinear, nonequilibrium and collective dynamics in aperiodically modulated cold atom system, Phys. Rep. **698**, 1 (2017).

[4] J. G. Ramírez, A. C. Basaran, J. de la Venta, J. Pereiro, and I. K. Schuller, Magnetic field modulated microwave spectroscopy across phase transitions and the search for new superconductors, Rep. Prog. Phys. **77**, 093902 (2014).

[5] P. Liu, B. Lei, X. H. Chen, L. Wang, and X. L. Wang, Superior carrier tuning in ultrathin superconducting materials by electric-field gating, Nat. Rev. Phys. **4**, 336 (2022).

[6] J. G. Horstmann, H. Böckmann, B. Wit, F. Kurtz, G. Storeck, and C. Ropers, Coherent control of a surface structural phase transition, Nature (London) **583**, 232 (2020).

[7] P. H. Fu, Y. Xu, X. L. Yu, J. F. Liu, and J. S. Wu, Electrically modulated Josephson junction of light-dressed topological insulators, Phys. Rev. B **105**, 064503 (2022).

[8] Y. S. Lu, J. L. Li, and C. T. Wu, Topological phase transitions of Dirac magnons in honeycomb ferromagnets, Phys. Rev. Lett. **127**, 217202 (2021).

[9] S. Zhang, G. Go, K. J. Lee, and S. K. Kim, SU(3) topology of magnon-phonon hybridization in 2D antiferromagnets, Phys. Rev. Lett. **124**, 147204 (2020).

[10] X. Zhang, Y. H. Zhang, S. Okamoto, and D. Xiao, Thermal Hall effect induced by magnon-phonon interactions, Phys. Rev. Lett. **123**, 167202 (2019).

[11] E. Thingstad, A. Kamra, A. Brataas, and A. Sudbø, Chiral phonon transport induced by topological magnons, Phys. Rev. Lett. **122**, 107201 (2019).

[12] K. S. Kim, K. H. Lee, S. B. Chung, and J. G. Park, Magnon topology and thermal Hall effect in trimerized triangular lattice antiferromagnet, Phys. Rev. B **100**, 064412 (2019).

[13] Y. L. Lu, X. Guo, V. Koval, and C. L. Jia, Topological thermal Hall effect driven by spin-chirality fluctuations in frustrated antiferromagnets, Phys. Rev. B **99**, 054409 (2019).

[14] J. Romhányi, K. Penc, and R. Ganesh, Hall effect of triplons in a dimerized quantum magnet, Nat. Commun. **6**, 6805 (2015).

[15] M. Kenzelmann, A. B. Harris, S. Jonas, C. Broholm, J. Schefer, S. B. Kim, C. L. Zhang, S.-W. Cheong, O. P. Vajk, and J. W. Lynn, Magnetic inversion symmetry breaking and ferroelectricity in $TbMnO_3$, Phys. Rev. Lett. **95**, 087206 (2005).

[16] B. Ruette, S. Zvyagin, A. P. Pyatakov, A. Bush, J. F. Li, V. I. Belotelov, A. K. Zvezdin, and D. Viehland, Magnetic-field-induced phase transition in $BiFeO_3$ observed by high-field electron spin resonance: Cycloidal to homogeneous spin order, Phys. Rev. B **69**, 064114 (2004).

[17] G. L. Ge, C. Shi, C. K. Chen, Y. J. Shi, F. Yan, H. R. Bai, J. Yang, J. F. Lin, B. Shen, and J. W. Zhai, Tunable domain switching features of incommensurate antiferroelectric ceramics realizing excellent energy storage properties, Adv. Mater. **34**, 2201333 (2022).

[18] X. L. Tan, C. Ma, J. Frederick, S. Beckman, and K. G. Webber, The antiferroelectric ↔ ferroelectric phase transition in lead-containing and lead-free perovskite ceramics, J. Am. Ceram. Soc. **94**, 4091 (2011).

[19] C. M. Bender and S. Boettcher, Real spectra in non-Hermitian Hamiltonians having $\mathscr{P}\mathscr{T}$ symmetry, Phys. Rev. Lett. **80**, 5243 (1998).

[20] J. M. Wen, X. S. Jiang, L. Jiang, and M. Xiao, Parity-time symmetry in optical microcavity systems, J. Phys. B: At. Mol. Opt. Phys. **51**, 222001 (2018).

[21] A. A. Zyablovsky, A. P. Vinogradov, A. A. Pukhov, A. V. Dorofeenko, and A. A. Lisyansky, PT-symmetry in optics, J. Phys. B: At. Mol. Opt. Phys. **57**, 1063 (2014).

[22] H. Fan, J. Y. Chen, Z. T. Zhao, J. M. Wen, and Y. P. Huang, Antiparity-time symmetry in passive nanophotonics, ACS Photonics **7**, 3035 (2020).

[23] Y. H. Lai, Y. Kun Lu, M. G. Suh, Z. Q. Yuan, and K. Vahala, Observation of the exceptional-point-enhanced Sagnac effect, Nature (London) **576**, 65 (2019).

[24] H. Hodaei, M. A. Miri, M. Heinrich, D. N. Christodoulides, and M. Khajavikhan, Parity-time–symmetric microring lasers, Science **346**, 975 (2014).

[25] M. D. Wang, S. Liu, Q. Y. Ma, R. Y. Zhang, D. Y. Wang, Q. H. Guo, B. Yang, M. Z. Ke, Z. Y. Liu, and C. T. Chan, Experimental observation of non-Abelian earring nodal links in phononic crystals, Phys. Rev. Lett. **128**, 246601 (2022).

[26] Y. Aurégan and V. Pagneux, $\mathcal{PT}$-symmetric scattering in flow duct acoustics, Phys. Rev. Lett. **118**, 174301 (2017).

[27] X. F. Zhu, H. Ramezani, C. Z. Shi, J. Zhu, and X. Zhang, $\mathcal{PT}$-symmetric acoustics, Phys. Rev. X **4**, 031042 (2014).

[28] X. Yang, J. W. Li, Y. F. Ding, M. W. Xu, X. F. Zhu, and J. Zhu, Observation of transient parity-time symmetry in electronic systems, Phys. Rev. Lett. **128**, 065701 (2022).

[29] S. Assawaworrarit and S. H. Fan, Robust and efficient wireless power transfer using a switch-mode implementation of a nonlinear parity–time symmetric circuit, Nat. Electron. **3**, 273 (2020).

[30] Z. Y. Dong, Z. P. Li, F. Y. Yang, C. W. Qiu, and J. S. Ho, Sensitive readout of implantable microsensors using a wireless system locked to an exceptional point, Nat. Electron. **2**, 335 (2019).

[31] J. L. Zhou, B. Zhang, W. X. Xiao, D. Y. Qiu, and Y. F. Chen, Nonlinear parity-time-symmetric model for constant efficiency wireless power transfer: Application to a drone-in-flight wireless charging platform, IEEE Trans. Ind. Electron. **66**, 4097 (2019).

[32] J. Schindler, Z. Lin, J. M. Lee, H. Ramezani, F. M. Ellis, and T. Kottos, $\mathcal{PT}$-symmetric electronics, J. Phys. A: Math. Theor. **45**, 444029 (2012).

[33] M. Parto, Y. Z. G. N. Liu, B. Bahari, M. Khajavikhan, and D. N. Christodoulides, Non-Hermitian and topological photonics: Optics at an exceptional point, Nanophotonics **10**, 403 (2021).

[34] H. Li, A. Mekawy, A. Krasnok, and A. Alù, Virtual parity-time symmetry, Phys. Rev. Lett. **124**, 193901 (2020).

[35] M. Kremer, T. Biesenthal, L. J. Maczewsky, M. Heinrich, R. Thomale, and A. Szameit, Demonstration of a two-dimensional $\mathcal{PT}$-symmetric crystal, Nat. Commun. **10**, 435 (2019).

[36] H. Zhao and L. Feng, Parity–time symmetric photonics, Natl. Sci. Rev. **5**, 183 (2018).

[37] X. Ni, D. Smirnova, A. Poddubny, D. Leykam, Y. Chong, and A.B. Khanikaev, $\mathcal{PT}$ phase transitions of edge states at $\mathcal{PT}$

symmetric interfaces in non-Hermitian topological insulators, Phys. Rev. B **98**, 165129 (2018).

[38] S. V. Suchkov, A. A. Sukhorukov, J. H. Huang, S. V. Dmitriev, C. H. Lee, and Y. S. Kivshar, Nonlinear switching and solitons in PT-symmetric photonic systems, Laser Photonics Rev. **10**, 177 (2016).

[39] J. H. Li, J. H. Li, Q. Xiao, and Y. Wu, Giant enhancement of optical high-order sideband generation and their control in a dimer of two cavities with gain and loss, Phys. Rev. A **93**, 063814 (2016).

[40] L. Y. He, Parity-time-symmetry–enhanced sideband generation in an optomechanical system, Phys. Rev. A **99**, 033843 (2019).

[41] L. Li, W. X. Yang, Y. X. Zhang, T. Shui, A. X. Chen, and Z. M. Jiang, Enhanced generation of charge-dependent second-order sideband and high-sensitivity charge sensors in a gain-cavity-assisted optomechanical system, Phys. Rev. A **98**, 063840 (2018).

[42] M. Lawrence, N. N. Xu, X. Q. Zhang, L. Q. Cong, J. G. Han, W. L. Zhang, and S. Zhang, Manifestation of PT symmetry breaking in polarization space with terahertz metasurfaces, Phys. Rev. Lett. **113**, 093901 (2014).

[43] Y. Sun, W. Tan, H.-Q. Li, J. S. Li, and H. Chen, Experimental demonstration of a coherent perfect absorber with PT phase transition, Phys. Rev. Lett. **112**, 143903 (2014).

[44] W. D. Heiss, The physics of exceptional points, J. Phys. A: Math. Theor. **45**, 444016 (2012).

[45] J. H. Li, X. G. Zhan, C. L. Ding, D. Zhang, and Y. Wu, Enhanced nonlinear optics in coupled optical microcavities with an unbroken and broken parity-time symmetry, Phys. Rev. A **92**, 043830 (2015).

[46] Y. H. Li, C. Liang, C. Y. Wang, C. C. Lu, and Y.-C. Liu, Gain-loss-induced hybrid skin-topological effect, Phys. Rev. Lett. **128**, 223903 (2022).

[47] W.-C. Wang, Y.-L. Zhou, H.-L. Zhang, J. Zhang, M.-C. Zhang, Y. Xie, C.-W. Wu, T. Chen, B.-Q. Ou, W. Wu, H. Jing, and P.-X. Chen, Observation of $\mathcal{PT}$-symmetric quantum coherence in a single-ion system, Phys. Rev. A **103**, L020201 (2021).

[48] A. Guo, G. J. Salamo, D. Duchesne, R. Morandotti, M. Volatier-Ravat, V. Aimez, G. A. Siviloglou, and D. N. Christodoulides, Observation of $\mathcal{PT}$-symmetry breaking in complex optical potentials, Phys. Rev. Lett. **103**, 093902 (2009).

[49] H. Jing, S. K. Özdemir, Z. Geng, J. Zhang, X.-Y. Lü, B. Peng, L. Yang, and F. Nori, Optomechanically-induced transparency in parity-time-symmetric microresonators, Sci. Rep. **5**, 9663 (2015).

[50] X. Zhou and Y. D. Chong, PT symmetry breaking and nonlinear optical isolation in coupled microcavities, Opt. Ex. **24**, 257590 (2016).

[51] B. Peng, Ş. Kaya Özdemir, F. C. Lei, F. Monifi, M. Gianfreda, G. L. Long, S. H. Fan, F. Nori, C. M. Bender, and L. Yang, Parity–time-symmetric whispering-gallery microcavities, Nat. Phys. **10**, 394 (2014).

[52] L. Feng, M. Ayache, J. Q. Huang, Y.-L. Xu, M.-H. Lu, Y.-F. Chen, Y. Fainman, and A. Scherer, Nonreciprocal light propagation in a silicon photonic circuit, Science **333**, 729 (2011).

[53] L. Jin, X. Z. Zhang, G. Zhang, and Z. Song, Reciprocal and unidirectional scattering of parity-time symmetric structures, Sci. Rep. **6**, 20976 (2016).

[54] S. Weimann, M. Kremer, Y. Plotnik, Y. Lumer, S. Nolte, K. G. Makris, M. Segev, M. C. Rechtsman, and A. Szameit, Topologically protected bound states in photonic parity–time-symmetric crystals, Nat. Mater. **16**, 433 (2017).

[55] Y. Huang, Y. C. Shen, C. J. Min, S. H. Fan, and G. Veronis, Unidirectional reflectionless light propagation at exceptional points, Nanophotonics **6**, 977 (2017).

[56] A. Regensburger, C. Bersch, M.-A. Miri, G. Onishchukov, D. N. Christodoulides, and U. Peschel, Parity–time synthetic photonic lattices, Nature (London) **488**, 167 (2012).

[57] Z. Lin, H. Ramezani, T. Eichelkraut, T. Kottos, H. Cao, and D. N. Christodoulides, Unidirectional invisibility induced by $\mathcal{PT}$-symmetric periodic structures, Phys. Rev. Lett. **106**, 213901 (2011).

[58] H. Ramezani, T. Kottos, R. El-Ganainy, and D. N. Christodoulides, Unidirectional nonlinear $\mathcal{PT}$-symmetric optical structures, Phys. Rev. A **82**, 043803 (2010).

[59] X. X. Zhou, X. Lin, Z. C. Xiao, T. Low, A. Alù, B. L. Zhang, and H. D. Sun, Controlling photonic spin Hall effect via exceptional points, Phys. Rev. B **100**, 115429 (2019).

[60] L. Feng, Z. J. Wong, R.-M. Ma, Y. Wang, and X. Zhang, Single-mode laser by parity-time symmetry breaking, Science **346**, 972 (2014).

[61] Z. J. Wong, Y.-L. Xu, J. Kim, K. O'Brien, Y. Wang, L. Feng, and X. Zhang, Lasing and anti-lasing in a single cavity, Nature Photon **10**, 796 (2016).

[62] Y. X. Zhang, C. R. I. Carceller, M. Kjaergaard, and A. S. Sørensen, Charge-noise insensitive chiral photonic interface for waveguide circuit QED, Phys. Rev. Lett. **127**, 233601 (2021).

[63] A. Blais, R.-S. Huang, A. Wallraff, S. M. Girvin, and R. J. Schoelkopf, Cavity quantum electrodynamics for superconducting electrical circuits: An architecture for quantum computation, Phys. Rev. A **69**, 062320 (2004).

[64] A. Blais, A. L. Grimsmo, S. M. Girvin, and A. Wallraff, Circuit quantum electrodynamics, Rev. Mod. Phys. **93**, 025005 (2021).

[65] J. Koch, A. A. Houck, K. L. Hur, and S. M. Girvin, Time-reversal-symmetry breaking in circuit-QED-based photon lattices, Phys. Rev. A **82**, 043811 (2010).

[66] X. Wang and H. R. Li, Chiral quantum network with giant atoms, Quantum Sci. Technol. **7**, 035007 (2022).

[67] X. Gu, A. F. Kockum, A. Miranowicz, Y.-X. Liu, and F. Nori, Microwave photonics with superconducting quantum circuits, Phys. Rep. **718-719**, 1 (2017).

[68] B. Peropadre, D. Zueco, F. Wulschner, F. Deppe, A. Marx, R. Gross, and J. J. G. Ripoll, Tunable coupling engineering between superconducting resonators: From sidebands to effective gauge fields, Phys. Rev. B **87**, 134504 (2013).

[69] P. Bertet, C. J. P. M. Harmans, and J. E. Mooij, Parametric coupling for superconducting qubits, Phys. Rev. B **73**, 064512 (2006).

[70] W. Xiong, D.-Y. Jin, J. Jing, C.-H. Lam, and J. Q. You, Controllable coupling between a nanomechanical resonator and a coplanar-waveguide resonator via a superconducting flux qubit, Phys. Rev. A **92**, 032318 (2015).

[71] L. Dong and C. Huang, Double-hump solitons in fractional dimensions with a $\mathcal{PT}$-symmetric potential, Opt. Express **26**, 10509 (2018).

[72] K. Li, D. A. Zezyulin, V. V. Konotop, and P. G. Kevrekidis, Parity-time-symmetric optical coupler with birefringent arms, Phys. Rev. A **87**, 033812 (2013).

[73] L. Qin, C. Hang, and G. X. Huang, Controllable $\mathcal{PT}$ phase transition and asymmetric soliton scattering in atomic gases with linear and nonlinear potentials, Phys. Rev. A **99**, 043832 (2019).

[74] D. F. Walls and G. J. Milburn, *Quantum Optics* (Springer-Verlag, Berlin, 1994).

[75] C. W. Gardiner and P. Zoller, *Quantum Noise* (Springer-Verlag, Berlin, 2004).

[76] E. J. Weniger, J. Čížek, and F. Vinette, The summation of the ordinary and renormalized perturbation series for the ground state energy of the quartic, sextic, and octic anharmonic oscillators using nonlinear sequence transformations, J. Math. Phys. **34**, 571 (1993).

[77] J. F. Stanton and J. Gauss, Perturbative treatment of the similarity transformed Hamiltonian in equation-of-motion coupled-cluster approximations, J. Chem. Phys. **103**, 1064 (1995).

[78] H.-P. Breuer, D. Burgarth, and F. Petruccione, Non-Markovian dynamics in a spin star system: Exact solution and approximation techniques, Phys. Rev. B **70**, 045323 (2004).

[79] R. W. Boyd, *Nonlinear Optics* (Academic, New York, 2020).

[80] E. Waks and J. Vuckovic, Dipole induced transparency in drop-filter cavity-waveguide systems, Phys. Rev. Lett. **96**, 153601 (2006).

[81] D. Englund, A. Faraon, I. Fushman, N. Stoltz, P. Petroff, and J. Vučković, Controlling cavity reflectivity with a single quantum dot, Nature (London) **450**, 857 (2007).

[82] I. Fushman, D. Englund, A. Faraon, N. Stoltz, P. Petroff, and J. Vučković, Controlled phase shifts with a single quantum dot, Science **320**, 769 (2008).

[83] A. Faraon, I. Fushman, D. Englund, N. Stoltz, P. Petroff, and J. Vučković, Dipole induced transparency in waveguide coupled photonic crystal cavities, Opt. Express **16**, 12154 (2008).

[84] B. C. Ren, G. Y. Wang, and F. G. Deng, Universal hyperparallel hybrid photonic quantum gates with dipole-induced transparency in the weak-coupling regime, Phys. Rev. A **91**, 032328 (2015).

[85] M. M. Salour, Quantum interference effects in two-photon spectroscopy, Rev. Mod. Phys. **50**, 667 (1978).

[86] P. M. R. Brydon, D. S. L. Abergel, D. F. Agterberg, and V. M. Yakovenko, Loop currents and anomalous Hall effect from time-reversal symmetry-breaking superconductivity on the honeycomb lattice, Phys. Rev. X **9**, 031025 (2019).

[87] D. Boyanovsky and D. Jasnow, Coherence of mechanical oscillators mediated by coupling to different baths, Phys. Rev. A **96**, 012103 (2017).

[88] R. W. Simmonds, K. M. Lang, D. A. Hite, S. Nam, D. P. Pappas, and J. M. Martinis, Decoherence in Josephson phase qubits from junction resonators, Phys. Rev. Lett. **93**, 077003 (2004).

[89] M. S. Allman, F. Altomare, J. D. Whittaker, K. Cicak, D. Li, A. Sirois, J. Strong, J. D. Teufel, and R. W. Simmonds, rf-SQUID-mediated coherent tunable coupling between a superconducting phase qubit and a lumped-element resonator, Phys. Rev. Lett. **104**, 177004 (2010).

[90] M. S. Allman, J. D. Whittaker, M. Castellanos-Beltran, K. Cicak, F. da Silva, M. P. DeFeo, F. Lecocq, A. Sirois, J. D. Teufel, J. Aumentado, and R. W. Simmonds, Tunable resonant and nonresonant interactions between a phase qubit and LC resonator, Phys. Rev. Lett. **112**, 123601 (2014).

[91] R. Harris, A. J. Berkley, M. W. Johnson, P. Bunyk, S. Govorkov, M. C. Thom, S. Uchaikin, A. B. Wilson, J. Chung, E. Holtham, J. D. Biamonte, A. Yu. Smirnov, M. H. S. Amin, and A. M. van den Brink, Signand magnitude-tunable coupler for superconducting flux qubits, Phys. Rev. Lett. **98**, 177001 (2007).

[92] Y. Zhang, Y.-Q. Ge, and Y.-X. Liu, Simulation of Kitaev model using one-dimensional chain of superconducting qubits and environmental effect on topological states, arXiv:2302.03834.

[93] F. Yoshihara, T. Fuse, Z. Ao, S. Ashhab, K. Kakuyanagi, S. Saito, T. Aoki, K. Koshino, and K. Semba, Inversion of qubit energy levels in qubit-oscillator circuits in the deep-strong-coupling regime, Phys. Rev. Lett. **120**, 183601 (2018).

[94] F. Yoshihara, T. Fuse, S. Ashhab, K. Kakuyanagi, S. Saito, and K. Semba, Superconducting qubit–oscillator circuit beyond the ultrastrong-coupling regime, Nat. Phys. **13**, 44 (2017).

[95] I. C. Hoi, C. M. Wilson, G. Johansson, T. Palomaki, B. Peropadre, and P. Delsing, Demonstration of a single-photon router in the microwave regime, Phys. Rev. Lett. **107**, 073601 (2011).

[96] T. Noh, Z. Xiao, X. Y. Jin, K. Cicak, E. Doucet, J. Aumentado, L. C. G. Govia, L. Ranzani, A. Kamal, and R. W. Simmonds, Strong parametric dispersive shifts in a statically decoupled two-qubit cavity QED system, Nat. Phys. **19**, 1445 (2023).

[97] J. Stehlik, D. M. Zajac, D. L. Underwood, T. Phung, J. Blair, S. Carnevale, D. Klaus, G. A. Keefe, A. Carniol, M. Kumph *et al.*, Tunable coupling architecture for fixed-frequency transmon superconducting qubits, Phys. Rev. Lett. **127**, 080505 (2021).

[98] Y. Xu, J. Chu, J. Yuan, J. Qiu, Y. Zhou, L. Zhang, X. Tan, Y. Yu, S. Liu, J. Li *et al.*, High-fidelity, high-scalability two-qubit gate scheme for superconducting qubits, Phys. Rev. Lett. **125**, 240503 (2020).

[99] A. Kandala, K. X. Wei, S. Srinivasan, E. Magesan, S. Carnevale, G. A. Keefe, D. Klaus, O. Dial, and D. C. McKay, Demonstration of a high-fidelity CNOT gate for fixed-frequency transmons with engineered ZZ suppression, Phys. Rev. Lett. **127**, 130501 (2021).

[100] R. Harris, T. Lanting, A. J. Berkley, J. Johansson, M. W. Johnson, P. Bunyk, E. Ladizinsky, N. Ladizinsky, T. Oh, and S. Han, Compound Josephson-junction coupler for flux qubits with minimal crosstalk, Phys. Rev. B **80**, 052506 (2009).

[101] I. Ozfidan, C. Deng, A. Y. Smirnov, T. Lanting, R. Harris, L. Swenson, J. Whittaker, F. Altomare, M. Babcock, C. Baron, A. J. Berkley, K. Boothby *et al.*, Demonstration of a nonstoquastic Hamiltonian in coupled superconducting flux qubits, Phys. Rev. Appl. **13**, 034037 (2020).

[102] B.-M. Ann, S. Deve, and G. A. Steele, Resolving nonperturbative renormalization of a microwave-dressed weakly

anharmonic superconducting qubit coupled to a single quantized mode, Phys. Rev. Lett. **131**, 193605 (2023).

[103] C. M. Wilson, T. Duty, F. Persson, M. Sandberg, G. Johansson, and P. Delsing, Coherence times of dressed states of a superconducting qubit under extreme driving, Phys. Rev. Lett. **98**, 257003 (2007).

[104] V. S. Ilchenko, A. A. Savchenkov, A. B. Matsko, and L. Maleki, Nonlinear optics and crystalline whispering gallery mode cavities, Phys. Rev. Lett. **92**, 043903 (2004).

[105] Th. K. Mavrogordatos, G. Tancredi, M. Elliott, M. J. Peterer, A. Patterson, J. Rahamim, P. J. Leek, E. Ginossar, and M. H. Szymańska, Simultaneous bistability of a qubit and resonator in circuit quantum electrodynamics, Phys. Rev. Lett. **118**, 040402 (2017).

[106] X. He, P. Pakkiam, A. A. Gangat, M. J. Kewming, G. J. Milburn, and A. Fedorov, Effect of measurement backaction on quantum clock precision studied with a superconducting circuit, Phys. Rev. Appl. **20**, 034038 (2023).

[107] S.-F. Qi and J. Jing, Generation of Bell and Greenberger-Horne-Zeilinger states from a hybrid qubit-photon-magnon system, Phys. Rev. A **105**, 022624 (2022).

[108] B. T. Gard, K. Jacobs, R. McDermott, and M. Saffman, Microwave-to-optical frequency conversion using a cesium atom coupled to a superconducting resonator, Phys. Rev. A **96**, 013833 (2017).

[109] J. I. Cirac, M. Lewenstein, and P. Zoller, Laser cooling a trapped atom in a cavity: Bad-cavity limit, Phys. Rev. A **51**, 1650 (1995).

[110] J. I. Cirac, Interaction of a two-level atom with a cavity mode in the bad-cavity limit, Phys. Rev. A **46**, 4354 (1992).

[111] J. Zakrzewski and M. Lewenstein, Theory of dressed-state lasers in the bad-cavity limit, Phys. Rev. A **45**, 2057 (1992).

[112] H.-K. Lau and A. A. Clerk, Ground-state cooling and high-fidelity quantum transduction via parametrically driven bad-cavity optomechanics, Phys. Rev. Lett. **124**, 103602 (2020).